Climatology and Environmental Characteristics of Extreme Precipitation Events in the Southeastern United States

BENJAMIN J. MOORE,* KELLY M. MAHONEY, AND ELLEN M. SUKOVICH

Cooperative Institute for Research in Environmental Sciences, University of Colorado Boulder, and Physical Sciences Division, NOAA/Earth System Research Laboratory, Boulder, Colorado

ROBERT CIFELLI AND THOMAS M. HAMILL

Physical Sciences Division, NOAA/Earth System Research Laboratory, Boulder, Colorado

ABSTRACT

This paper documents the characteristics of extreme precipitation events (EPEs) in the southeastern United States (SEUS) during 2002–11. The EPEs are identified by applying an object-based method to 24-h precipitation analyses from the NCEP stage-IV dataset. It is found that EPEs affected the SEUS in all months and occurred most frequently in the western portion of the SEUS during the cool season and in the eastern portion during the warm season. The EPEs associated with tropical cyclones, although less common, tended to be larger in size, more intense, and longer lived than "nontropical" EPEs. Nontropical EPEs in the warm season, relative to those in the cool season, tended to be smaller in size and typically involved more moist, conditionally unstable conditions but weaker dynamical influences. Synoptic-scale composites are constructed for nontropical EPEs stratified by the magnitude of vertically integrated water vapor transport (IVT) to examine distinct scenarios for the occurrence of EPEs. The composite results indicate that "strong IVT" EPEs occur within high-amplitude flow patterns involving strong transport of moist, conditionally unstable air within the warm sector of a cyclone, whereas "weak IVT" EPEs occur within low-amplitude flow patterns featuring weak transport but very moist and conditionally unstable conditions. Finally, verification of deterministic precipitation forecasts from a reforecast dataset based on the NCEP Global Ensemble Forecast System reveals that weak-IVT EPEs were characteristically associated with lower forecast skill than strong-IVT EPEs. Based on these results, it is suggested that further research should be conducted to investigate the forecast challenges associated with EPEs in the SEUS.

1. Introduction

a. Motivation and objectives

Extreme precipitation events (EPEs) are a primary natural hazard in the southeastern United States (SEUS), often causing flooding that can result in loss of human life and costly damage to property, infrastructure, and agriculture. The SEUS can experience this class of event in all seasons in conjunction with a variety of atmospheric phenomena, such as landfalling tropical cyclones (TCs; e.g., Atallah and Bosart 2003; Shepherd et al. 2007; Konrad and Perry 2010; Knight and Davis 2009; Villarini and Smith 2010), extratropical baroclinic waves and cyclones (e.g., Maddox et al. 1979; Konrad 1997; Moore et al. 2012), and mesoscale convective systems (MCSs; e.g., Schumacher and Johnson 2006). Furthermore, the processes associated with EPEs in the SEUS are often influenced by the unique physical geography of the region. Examples of such processes include water vapor transport from surrounding ocean basins (e.g., Knippertz and Wernli 2010; Moore et al. 2012; Pfahl et al. 2014), orographic forcing along the Appalachian Mountains (e.g., Pontrelli et al. 1999), and lifting

* Current affiliation: Department of Atmospheric and Environmental Sciences, University at Albany, State University of New York, Albany, New York.

Corresponding author address: Benjamin J. Moore, Department of Atmospheric and Environmental Sciences, University at Albany, State University of New York, 1400 Washington Ave., Albany, NY 12208.
E-mail: bjmoore@albany.edu

along topographically induced baroclinic zones (e.g., Koch and Ray 1997; Atallah and Bosart 2003; Srock and Bosart 2009).

The large diversity of phenomena and processes associated with EPEs in the SEUS underlies the complex and challenging nature of quantitative precipitation forecasts (QPFs) for these events. The QPF challenges associated with EPEs in the SEUS form a central research focus of the National Oceanic and Atmospheric Administration (NOAA) Hydrometeorological Testbed–Southeast (HMT-SE). As a key step toward the QPF-related objectives of HMT-SE, this paper seeks to advance the current understanding of the climatological and environmental characteristics of EPEs in the SEUS and to provide a precursory examination of related QPF challenges.

Although a number of prior studies have investigated the climatological characteristics of EPEs affecting the SEUS in some form (e.g., Maddox et al. 1979; Keim 1996; Konrad 1997, 2001; Brooks and Stensrud 2000; Schumacher and Johnson 2006; Kunkel et al. 2012), gaps in knowledge pertaining to this class of event remain. One pervasive problem is that many of these studies have used rain gauge observations, which have inherent limitations due to the spacing between observing stations (typically 25–50 km in the SEUS). It is, therefore, likely that many events in prior rain gauge–based climatologies were undersampled or completely missed (e.g., Brooks and Stensrud 2000). Hitchens et al. (2012, 2013) demonstrated a solution to this problem by utilizing high-resolution gridded multisensor precipitation datasets with homogeneous spatial coverage to examine heavy hourly precipitation over portions of the central and eastern United States. In the current study, we utilize gridded 24-h precipitation analyses from, as in Hitchens et al. (2013), the National Centers for Environmental Prediction (NCEP) stage-IV multisensor precipitation dataset (Lin and Mitchell 2005) to construct a 10-yr (2002–11) climatology of EPEs in the SEUS. Our objectives in constructing this climatology are threefold: 1) to document the temporal, spatial, and environmental characteristics of EPEs; 2) to examine through composite analysis synoptic-scale patterns associated with EPEs; and 3) to briefly assess numerical model QPF skill associated with subsets of EPEs.

b. Background on extreme precipitation in the SEUS

Based upon the results of past studies (e.g., Maddox et al. 1979; Keim 1996; Schumacher and Johnson 2006; Kunkel et al. 2012; Prat and Nelson 2014), it is evident that the climatology of EPEs in the SEUS is characterized by a dichotomy between the cool season (~October–April) and warm season (~May–September). For these two portions of the year, EPE environments can generally be viewed as occupying different areas of a hypothetical "dynamics–thermodynamics" phase space such that dynamical influences [e.g., quasigeostrophic (QG) forcing of ascent, transport of water vapor by a low-level jet (LLJ)] and thermodynamical influences [e.g., convective available potential energy (CAPE); precipitable water (PW)] tend to be dominant for cool-season and warm-season events, respectively. These differences in environmental conditions are linked to differences in the geographical variability (e.g., Keim 1996; Prat and Nelson 2014) and to differences in precipitation amounts associated with EPEs (Konrad 2001). In addition, numerical model QPF skill tends to be greater for environments characterized by strong dynamical forcing than for those characterized by weak dynamical forcing, particularly when poorly resolved moist convective processes are involved (e.g., Stensrud and Fritsch 1994; Mullen and Buizza 2001; Fritsch and Carbone 2004; Jankov and Gallus 2004; Zhang et al. 2006; Schumacher and Davis 2010; Keil et al. 2014), suggesting a possible QPF skill disparity between cool-season and warm-season EPE scenarios.

During the cool season, extreme precipitation in the SEUS is predominantly produced in connection with synoptic-scale baroclinic waves and cyclones and their associated fronts (e.g., Maddox et al. 1979; Businger et al. 1990; Keim 1996; Konrad 2001; Schumacher and Johnson 2006; Kunkel et al. 2012; Pfahl and Wernli 2012). Baroclinic systems that produce extreme precipitation are often associated with high-amplitude large-scale flow patterns analogous to the Maddox et al. (1979) "synoptic" type flash-flood pattern. In this type of pattern, heavy precipitation is supported by the poleward transport of warm, moist air along a LLJ positioned ahead of a slow-moving cold front (e.g., Lackmann 2002; Mahoney and Lackmann 2007) into a strongly ascending poleward-moving airstream associated with a warm conveyor belt (e.g., Browning 1990; Wernli and Davies 1997; Pfahl et al. 2014). Additionally, water vapor fluxes into the region of heavy precipitation are sometimes concentrated within narrow, elongated corridors called "atmospheric rivers" (e.g., Newell et al. 1992; Zhu and Newell 1998; Ralph et al. 2004), which have been shown to support extreme flood-producing precipitation in the central and eastern United States (Moore et al. 2012; Lavers and Villarini 2013).

During the warm season, EPEs tend to occur in the SEUS within environments characterized by weak baroclinicity and moist, conditionally unstable conditions supportive of deep moist convection. Warm-season EPEs can, accordingly, occur in conjunction with weak baroclinic systems (e.g., Konrad 1997), diurnal convection

(e.g., Wallace 1975; Winkler et al. 1988), MCSs (e.g., Schumacher and Johnson 2006), and landfalling TCs (e.g., Atallah and Bosart 2003; Schumacher and Johnson 2006; Shepherd et al. 2007; Konrad and Perry 2010; Knight and Davis 2009; Villarini et al. 2014). The thermodynamic conditions conducive to EPEs in the SEUS during the warm season can be strongly modulated by the transport of moist air on the western side of the North Atlantic subtropical high (e.g., Henderson and Vega 1996; Li et al. 2011; Li et al. 2013).

Warm-season precipitation intensity and, correspondingly, convective activity maximize in the SEUS during the afternoon concurrent with the peak in diurnal heating (e.g., Wallace 1975; Winkler et al. 1988; Parker and Ahijevych 2007; Carbone and Tuttle 2008; Prat and Nelson 2014). Diurnally forced convection is commonly initiated near mesoscale surface boundaries or convergence zones (e.g., Koch and Ray 1997; Konrad 1997), which may be linked to, for example, sea-breeze circulations (e.g., Carbone and Tuttle 2008), areas of cold-air damming east of the Appalachian Mountains (Bell and Bosart 1988; Bailey et al. 2003), or convectively generated cold pools. Given sufficient moisture, instability, and lifting, convection can be sustained, potentially resulting in extreme precipitation. In addition, coherent episodes of convective activity that do not adhere to the diurnal cycle can occur in the SEUS in association with MCSs originating along the Appalachian Mountains or, in some cases, propagating into the region from the central United States (Carbone et al. 2002; Parker and Ahijevych 2007).

2. Data and methods

a. Key datasets

A climatology of EPEs in the SEUS during 2002–11 was constructed using the NCEP stage-IV multisensor precipitation dataset. The stage-IV analysis is generated in real time with a combination of radar and rain gauge reports and comprises a continuous time series of high-resolution (~4 km) precipitation observations over the entire conterminous United States from 2002 to the present at 1-, 6-, and 24-h temporal resolution. The 6- and 24-h precipitation analyses are subject to manual quality control at the NOAA/National Weather Service River Forecast Centers.

The NCEP Climate Forecast System Reanalysis (CFSR; Saha et al. 2010) was utilized to investigate the environmental conditions associated with EPEs. The CFSR, produced at T382L64 spectral resolution, was obtained on a 0.5° latitude × 0.5° longitude global grid with 37 isobaric levels at 6-h temporal resolution. Numerical model QPF skill for subsets of EPEs was assessed

for the NOAA second-generation Global Ensemble Forecast System (GEFS) reforecast dataset (Hamill et al. 2013). This reforecast dataset consists of an extensive (1985–present) archive of 0–16-day 11-member global ensemble forecasts initialized daily using a fixed model configuration consistent with the 2012–14 version of the operational NCEP GEFS. Following Hamill (2012), the model forecasts were verified with the NCEP climatology-calibrated precipitation analysis (CCPA; Hou et al. 2014), which is generated through a linear regression of the stage-IV analyses to the daily gauge-based 0.25° NCEP Climate Prediction Center Unified Precipitation analyses (Higgins et al. 1996). The CCPA regression procedure has the effect of reducing biases in the stage-IV analyses, making the CCPA well suited for verifying the GEFS model forecasts, but can also result in reductions of extreme precipitation values (Hou et al. 2014), suggesting that the CCPA may be unsuitable for constructing the EPE climatology. The CCPA was obtained on a 0.125° grid and then upscaled to match the T254 (~0.5°) reforecast grid resolution.

b. Identification of EPEs from the stage-IV data

The first step in constructing a climatology of EPEs in the SEUS was to define the term "extreme." Several prior studies (e.g., Schumacher and Johnson 2005, 2006; Kunkel et al. 2012) have identified EPEs in the United States using the historical gauge-based recurrence interval precipitation thresholds calculated by Hershfield (1961), while others (e.g., Brooks and Stensrud 2000; Ralph and Dettinger 2012; Hitchens et al. 2012, 2013) have used fixed precipitation thresholds. We opted to use geographically varying upper quantiles of daily (24-h period ending 1200 UTC) precipitation amount, similar to Ralph et al. (2010) and Sukovich et al. (2014). Specifically, the 99th and 99.9th percentile values computed at each grid point for all days in all seasons during 2002–11 with >0 mm of precipitation (Fig. 1) were used as the basis for selecting EPEs.

Using the geographically varying thresholds, an object-based approach consistent with approaches in previous studies (e.g., Davis et al. 2006; Hitchens et al. 2012) was applied to identify candidate EPEs. The procedure for identifying EPEs from the stage-IV data involved the following steps:

1) For each 24-h precipitation analysis (ending 1200 UTC) during 2002–11 with precipitation amounts exceeding the 99th percentile value at more than one grid point within the "SEUS domain" (Fig. 1), the precipitation field covering the eastern United States (east of 100°W) was divided into sets of points above and below the 99th percentile threshold (Fig. 2). The
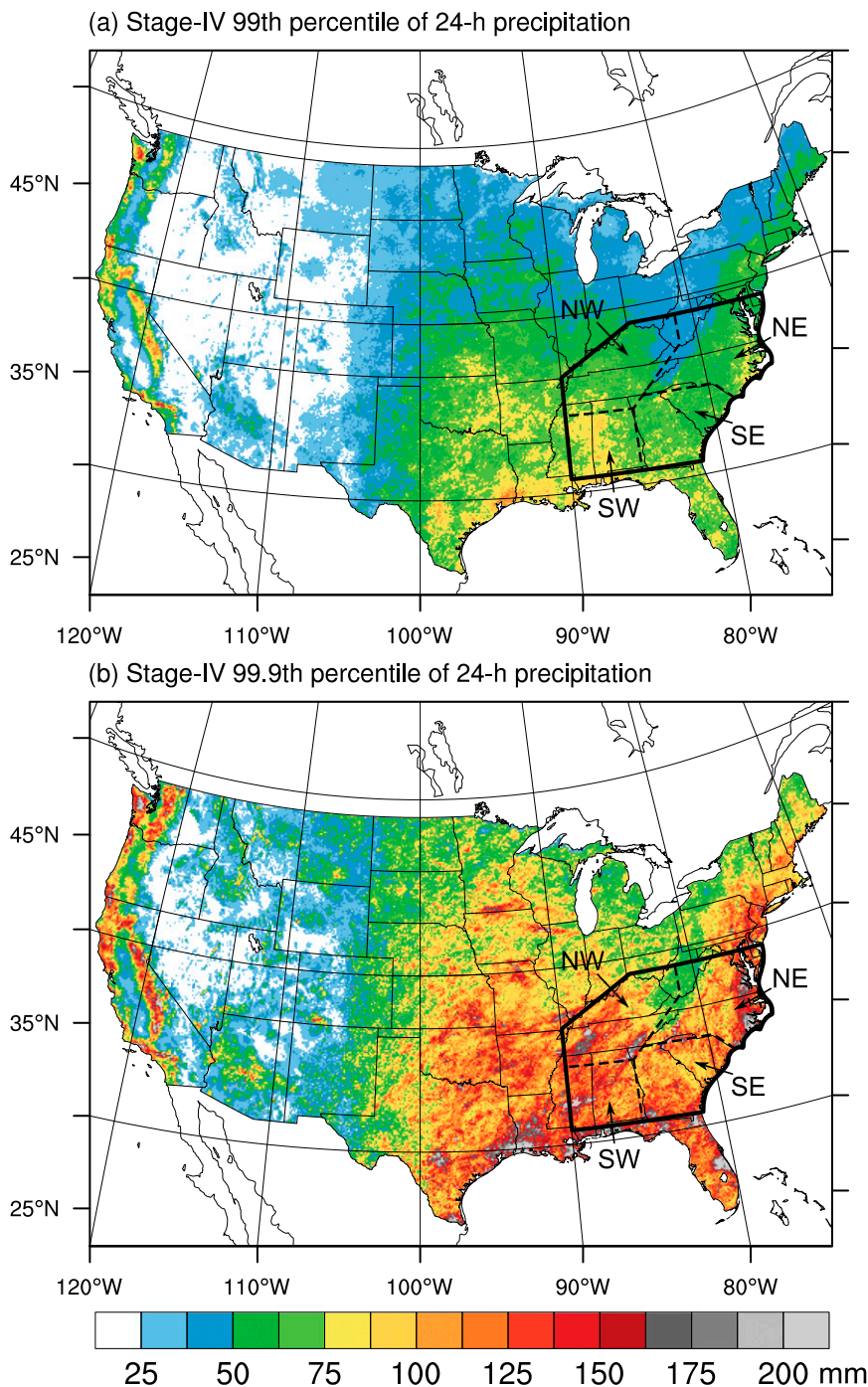
FIG. 1. Maps of (a) the 99th percentile and (b) the 99.9th percentile of 24-h precipitation (mm) calculated for all days in the stage-IV dataset during 2002–11 with >0 mm of precipitation. The thick black polygon denotes the boundaries of the SEUS domain, and the thin black lines mark the boundaries of the four regions within the SEUS domain. The regions are labeled (clockwise from top left) northwest (NW), northeast (NE), southeast (SE), and southwest (SW).
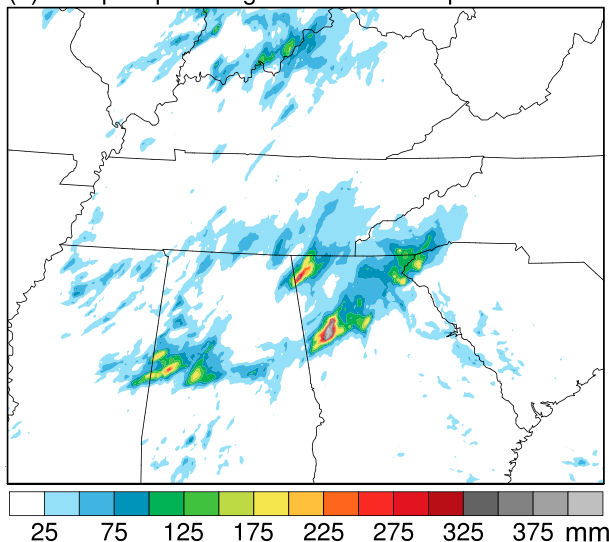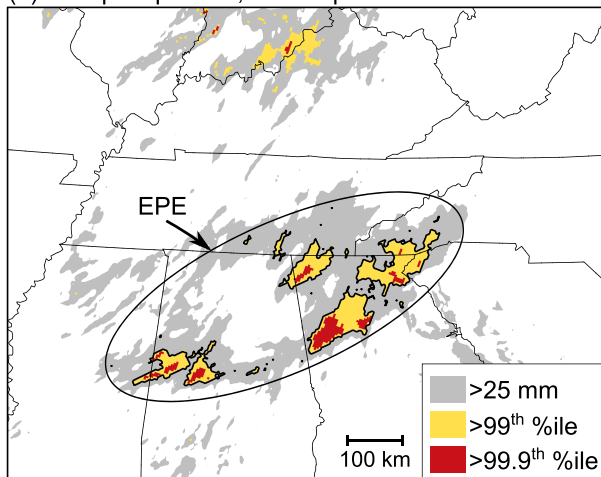
(a) 24-h precip. ending 1200 UTC 21 Sep 2009

(b) 24-h precip. >99th, >99.9th percentile

FIG. 2. Maps of the stage-IV 24-h precipitation accumulations ending at 1200 UTC 21 Sep 2009, showing (a) values shaded in mm according to the color bar and (b) values exceeding 25 mm (gray shading), the 99th percentile threshold (yellow shading), and the 99.9th percentile threshold (red shading). All of the extreme precipitation areas located within the ellipse in (b) together constitute one EPE object.

points above the 99th percentile threshold were considered extreme (yellow and red shading in Fig. 2b).

2) Areas of precipitation (or "precipitation objects") consisting of grid points separated by no more than 25 grid lengths (~100 km) were identified from the extreme precipitation field (i.e., yellow and red shaded regions enclosed in the ellipse in Fig. 2b). The ~100-km distance was allowed between grid points in order to group separate areas of extreme precipitation likely associated with the same weather system into the same precipitation object. Multiple

precipitation objects were allowed for a given 24-h period, and precipitation objects were permitted to extend beyond the borders of the SEUS domain.

3) For each precipitation object, the number of points specifically located *within the SEUS domain* that exceeded the 99th and 99.9th percentile thresholds, respectively, was determined. The precipitation objects were then ranked by both of these gridpoint counts, and only the objects with greater than the median number of points for both thresholds were retained. The median number was 183 grid points (~2928 km^2) for the 99th percentile and 8 grid points (~128 km^2) for 99.9th percentile. The exclusion of objects with less than the median number of grid points was done in an effort to eliminate spurious small-scale objects resulting from scattered convection or radar artifacts and to select only coherent events that affected the SEUS. Finally, only those precipitation objects for which ≥10% of the total number of grid points were located within the SEUS domain were retained. After this step, 293 precipitation objects remained (hereafter referred to as "EPE objects").

4) For the analysis presented in remainder of this paper, a set of temporally independent EPE objects (hereafter EPEs) was identified, resulting in a final EPE population of 274. For EPE objects from the same 24-h precipitation analysis, only the longest-duration EPE object was retained. Similarly, if ≥75% of the hours over the entire duration of an EPE object overlapped with the hours over the duration of another, only the longest-duration EPE object of the two was retained. This was done to account for EPEs spanning successive 24-h periods. The duration of each EPE object was estimated from hourly stage-IV analyses by conducting forward and backward searches in time from the hour of maximum precipitation for hours separated by ≤3 h during which the precipitation exceeded 10 mm h^{-1} at a minimum of five grid points within a 25 × 25 gridpoint box centered on the maximum 24-h precipitation location.[1] The duration was defined as the number of hours between the first and last times identified though this procedure. The resulting duration values, although sensitive to the specific criteria imposed above, provided realistic estimates of the duration of nearly continuous heavy rainfall associated with the EPE objects.

---

[1] Following Hitchens et al. (2012), hourly precipitation values of >104 mm were masked in the hourly stage-IV analyses in order to eliminate potentially spurious data values.

c. Regionalization of EPEs

The nontropical EPEs in the climatology were separated by region for the purpose of examining regional characteristics. To regionalize the EPEs, the SEUS domain was first divided into west and east regions, using the location of the spine of the Appalachian Mountains as an approximate guide in a similar manner to Konrad (1997). The west and east regions were then each separated into north and south regions. The four resulting regions (Fig. 1) were labeled northwest (NW), southwest (SW), northeast (NE), and southeast (SE). The region to which an EPE was assigned was the region containing the most extreme grid points associated with that EPE.

d. Stratification and composite analysis of EPEs

Each EPE was classified as either "tropical" or "nontropical" based upon whether it was produced in association with a TC. This classification was done manually using the NOAA National Hurricane Center best track dataset in combination with national radar imagery from the National Center for Atmospheric Research Mesoscale and Microscale Meteorology Division's Case Selection Image Archive (http://www.mmm.ucar.edu/imagearchive/). The EPEs that occurred in connection with a TC, including predecessor rain events (e.g., Galarneau et al. 2010; Moore et al. 2013), or the remnants of a TC were classified as tropical, and all others were classified as nontropical.

Given the diverse spectrum of synoptic-scale environments in which nontropical EPEs occur in the SEUS and the inherent QPF challenges therein, the composite analysis in this paper specifically focuses on nontropical EPEs. To produce physically meaningful composites, we adopted an approach of stratifying EPEs based on the degree of synoptic-scale dynamical "forcing" in their environments, as has similarly been done in the past for MCS environments (e.g., Evans and Doswell 2001). In particular, we focused on the dynamical forcing as it pertains to the horizontal transport of water vapor in the EPE environment, stratifying EPEs by the magnitude of the 1000–300-hPa vertically integrated water vapor transport (IVT), a measure of the total horizontal water vapor transport in the troposphere (e.g., Newell et al. 1992; Zhu and Newell 1998). To stratify the EPEs, the IVT magnitude, computed from the CFSR using the methodology of Neiman et al. (2008), was first temporally averaged over the 24-h (1200–1200 UTC) period corresponding to the EPE and then spatially averaged within a 5° latitude × 5° longitude box centered on the location of maximum 24-h precipitation for each EPE. The objective of this stratification approach was to distinguish environments in which the synoptic-scale flow drives strong horizontal transports of thermodynamic ingredients for heavy precipitation, from more quiescent environments that involve weak transports yet very moist, conditionally unstable conditions supportive of deep moist convection. Additionally, given that a major concern for operational forecasters and emergency managers when faced with a potential flooding scenario is the spatial extent of extreme precipitation amounts, we also stratified nontropical EPEs with respect to size, defined as the number of extreme grid points associated with an EPE.

Composites were generated using the CFSR for the top and bottom 50 (~23%) nontropical EPEs with respect to IVT magnitude and for the top and bottom 50 with respect to size. In addition, IVT-based composites were generated separately for the top and bottom quintile of nontropical EPEs for each of the four regions of the SEUS domain. Similar to Schumacher and Johnson (2005), Coniglio et al. (2010), and Moore et al. (2013), among others, the composites presented in this paper were generated in event-relative coordinates. Specifically, the grids associated with a given group of EPEs were shifted prior to compositing such that the locations of maximum 24-h precipitation were aligned with the mean location of maximum 24-h precipitation for that group. Geographic outlines and latitude–longitude marks are shown in the composites for spatial reference and scaling purposes. These map features are generally realistic for the regional composites, for which grids were shifted by relatively small distances. Composites were generated for the 6-h analysis time closest to the hour of maximum hourly precipitation associated with the EPE; if that hour was exactly halfway between two 6-h analysis times, the earlier analysis time was used.

A two-sided Student's t test (e.g., Wilks 2011) was performed for the composites of the top and bottom 50 EPEs with respect to IVT and size in order to test the null hypothesis that the mean for a given composite is equal to that of a composite of corresponding climatological (1979–2009) mean values. Following Narapusetty et al. (2009), a spectral method, involving a least squares fit of the 6-h CFSR data to the first four harmonics of the annual cycle, was used to compute the climatological means. Additionally, two-sided Student's t tests were performed to test for significant differences between the regional composites. To mitigate the effects of differing background conditions, prior to performing a t test for a given pair of regional subsets the climatological mean was subtracted from each field, and this difference was then normalized by the climatological standard deviation.

3. Climatology of EPEs in the SEUS

a. Interannual, monthly, and diurnal variability

Of the 274 EPEs that were identified through the procedures described in section 2b, 215 were classified as nontropical and 59 were classified as tropical. Considerable interannual variability was observed for both categories of EPEs (Fig. 3a), with 2002, 2003, 2009, and 2010 exhibiting a relatively large number of nontropical EPEs, and 2004 and 2005 exhibiting a relatively large number of tropical EPEs. Both 2004 and 2005 were characterized by unusually high Atlantic basin TC activity and were each host to particularly destructive and deadly hurricane seasons (Franklin et al. 2006; Beven et al. 2008). In 2002 there were significantly more nontropical EPEs than any other year; physical mechanisms to account for this result have not yet been investigated.

Nontropical EPEs occurred during all months of the year but exhibited a minimum in frequency during the winter, particularly in January and February, and a maximum in July (Fig. 3b). A similar monthly distribution of EPEs in the central and eastern United States has been documented by prior studies (e.g., Maddox et al. 1979; Brooks and Stensrud 2000; Schumacher and Johnson 2006; Hitchens et al. 2013). Strong-IVT EPEs occurred most frequently in spring and autumn and least frequently in summer, whereas weak-IVT EPEs occurred most frequently in summer and least frequently in winter (Fig. 3b). Consistent with the results of numerous studies (e.g., Wallace 1975; Winkler et al. 1988; Parker and Ahijevych 2007; Carbone and Tuttle 2008), EPE onset in summer occurred most frequently in the afternoon (not shown) concurrent with peak in diurnal heating, but in other seasons no clear preference was evident (not shown). Tropical EPEs occurred only during June–November and exhibited a prominent peak in frequency in September (Fig. 3b), consistent with the well-documented climatological peak in Atlantic basin TC activity during that month (e.g., Jiang and Zipser 2010).

b. Geographic variability

In aggregate, during 2002–11 EPEs in the SEUS occurred with greatest frequency within a broad corridor extending from northern Alabama and Georgia northeastward into western Virginia (Fig. 4a). Throughout the SEUS domain, EPEs accounted for a majority (nearly all in some locations) of the ~10–18 days during 2002–11 on which precipitation exceeded the 99th percentile (Fig. 4b). A majority of the EPEs occurring in the western portion of the SEUS domain were nontropical, with that category exhibiting the greatest frequency of occurrence across Mississippi, Alabama, Tennessee,
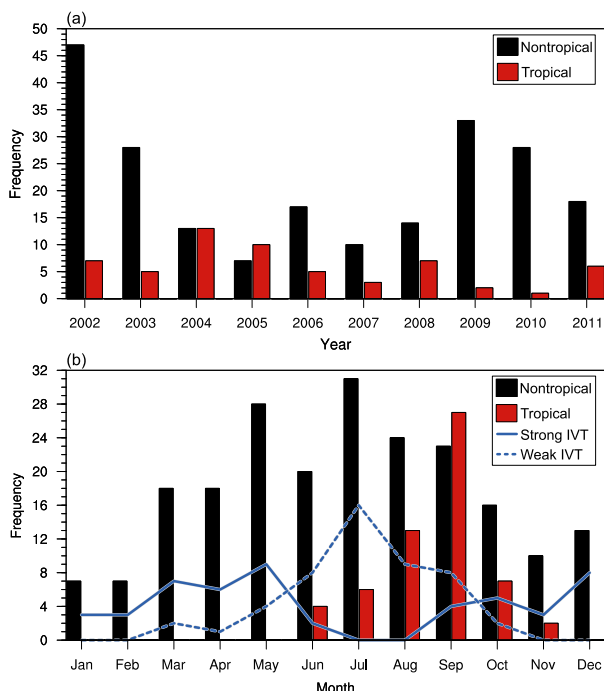

FIG. 3. The (a) yearly and (b) monthly distributions of nontropical (black) and tropical (red) EPEs. The monthly distributions of top 50 (strong IVT; solid blue line) and bottom 50 (weak IVT; dashed blue line) nontropical EPEs with respect to IVT magnitude are shown in (b).

Kentucky, and West Virginia (Fig. 4c). As will be discussed later, the size of nontropical EPEs varied substantially with respect to time of year. It is, therefore, possible that areas of greatest frequency in the western portion of the SEUS domain partially reflect areas where larger-scale nontropical EPEs preferentially occurred at certain times of the year.

Tropical EPEs occurred with greatest frequency in the eastern portion of the SEUS domain, with local areas of enhancement evident along the eastern slopes of the Appalachian Mountains and along the North Carolina and Virginia coastline (Fig. 4d). Consistent with these observations, a majority of the TCs that produced EPEs in the SEUS tracked along or across the eastern United States coast (not shown). The two aforementioned areas of enhancement highlight the influences of orography and coastal baroclinicity in focusing heavy precipitation as TCs track near the eastern United States coast (e.g., Atallah and Bosart 2003; Srock and Bosart 2009). Some TCs associated with tropical EPEs [e.g., TC Katrina (2005)] tracked across the Gulf of Mexico and subsequently into the southern United States, producing the large swaths of precipitation across the western portion of the SEUS domain (Fig. 4d).
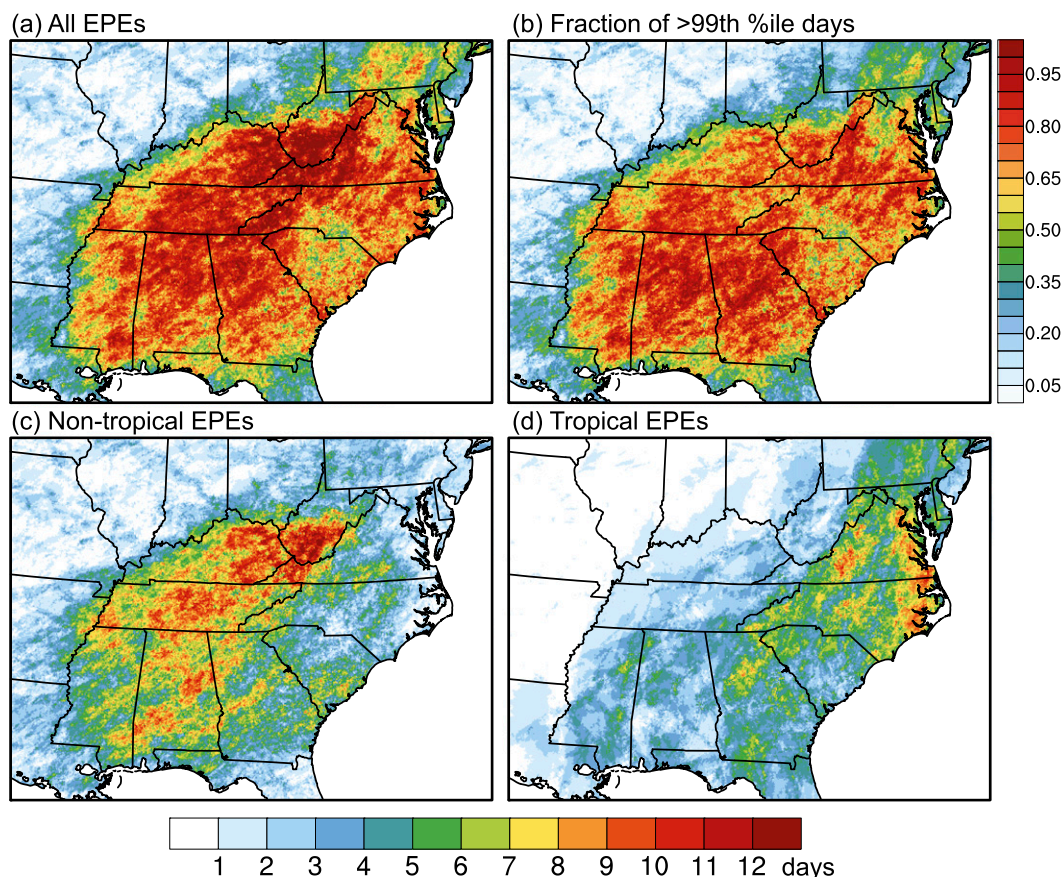
FIG. 4. Maps showing the number of days during 2002–11 on which precipitation exceeded the 99th percentile when an EPE was present for (a) all EPEs, (c) all nontropical EPEs, and (d) all tropical EPEs. (b) As in (a), but expressed as a fraction of the total number of days during 2002–11 on which the 99th percentile was exceeded.

Additional insight is obtained through an examination of the geographic distribution of EPE frequency as a function of season (Fig. 5). For December–February (DJF; Fig. 5a) and March–May (MAM; Fig. 5b), during which only nontropical EPEs were observed (see Fig. 3b), EPE frequency is highest across the western and southern portions of the domain. The areas of precipitation in DJF and MAM appear as elongated swaths, suggesting that EPEs in these seasons are relatively widespread and often occur in connection with synoptic-scale baroclinic waves. Accordingly, the climatological midlatitude baroclinic zone and the associated jet stream (i.e., the storm track) are positioned across the southern United States during DJF and MAM (Figs. 6a,b). In June–August (JJA), by contrast, EPEs occur most frequently in the eastern portion of the SEUS domain (Fig. 5c). Many areas of precipitation in JJA exhibit a somewhat speckled appearance, likely a signature of relatively disorganized convection tied to diurnal heating, while others appear as more coherent swaths that are likely related to TCs and MCSs. During JJA, the climatological subtropical high expands

poleward and westward across the eastern United States, and the midlatitude baroclinic zone and the jet stream are displaced poleward of the SEUS region, signaling a general absence of strong baroclinicity (Fig. 6c). In September–November (SON; Fig. 5d), the areas of greatest EPE frequency to first order correspond to the areas of greatest tropical EPE frequency displayed in Fig. 4d, highlighting the dominance of tropical EPEs during this season. Nonetheless, areas of large nontropical EPE frequency are also evident across the SEUS domain for SON (Fig. 5d). During SON, the climatological midlatitude baroclinic zone, previously displaced poleward of the SEUS during JJA, returns southward (Fig. 6d), suggesting that EPEs in this season often involve synoptic-scale baroclinic processes.

The monthly frequency distributions for nontropical EPEs occurring in the four regions of the SEUS domain (Fig. 7) exhibit characteristics that are consistent with those displayed in Fig. 5. For the NW region (63 events), EPE frequency maximizes prominently in May and minimizes in February. For the SW region (45 events), EPE
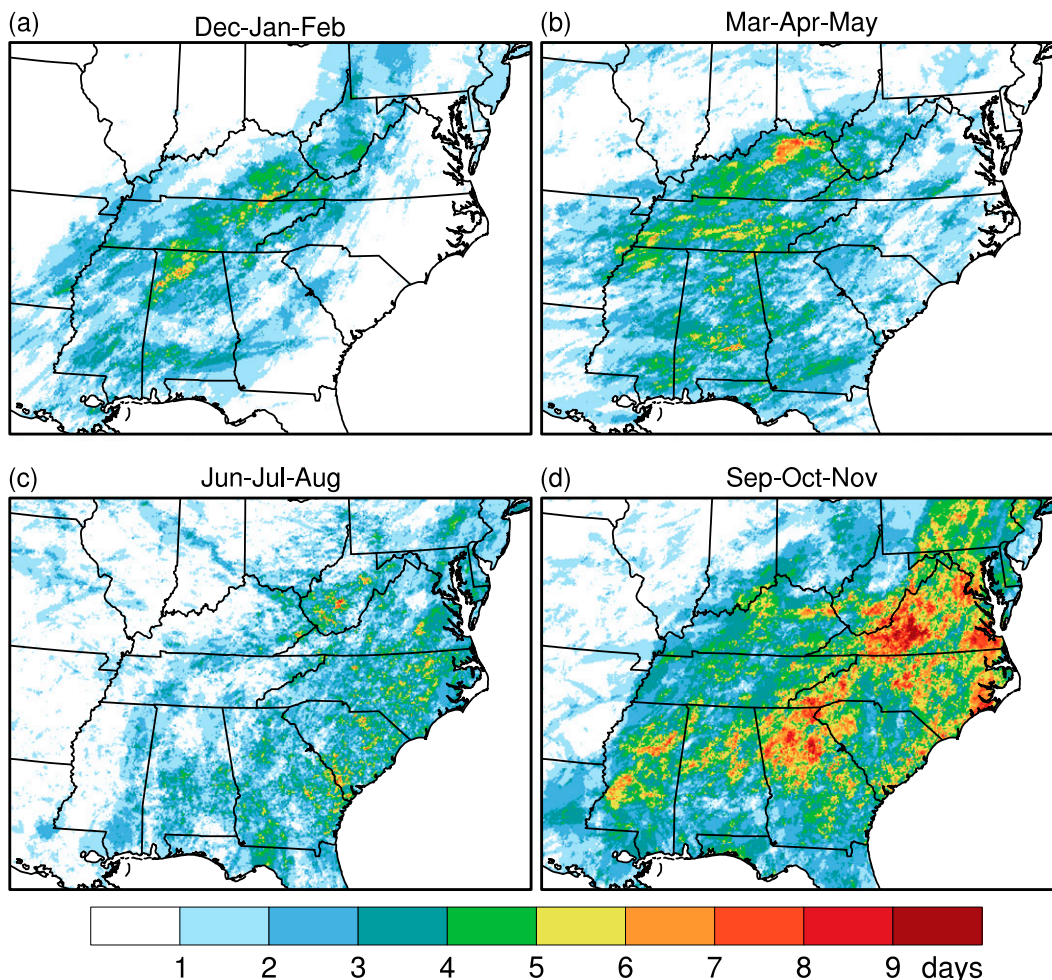
FIG. 5. As in Fig. 4a, but for (a) DJF, (b) MAM, (c) JJA, and (d) SON. The maps include both tropical and nontropical EPEs.

frequency maximizes in April and minimizes in August, with no EPEs occurring in that month. The NE region (46 events) and SE region (61 events) exhibit a maximum in EPE frequency in July and August, respectively, and a minimum during DJF. There is also a conspicuous peak in EPE frequency in March for the SE region.

c. Characteristics of EPEs

Considerable variability is evident with regard to the characteristics of the EPEs (Figs. 8 and 9). The distributions of size (i.e., number of extreme grid points associated with the EPE), average precipitation over all extreme grid points associated with an EPE, maximum 24-h precipitation amount, and duration are shown for nontropical and tropical EPEs in Fig. 8, with the monthly variability shown only for nontropical EPEs. For both categories, a large range in values is evident for these precipitation metrics, reflecting the diversity of events in the climatology. In general, tropical EPEs were larger in size, produced more precipitation, and were longer-lived than nontropical EPEs (rightmost two box-and-whisker plots in Figs. 8a–d). The differences in the means for all four precipitation metrics between tropical and nontropical EPEs are statistically significant above the 95% confidence level according to a two-sided Student's t test. Among nontropical EPEs, those occurring in JJA tended to be significantly (above the 95% confidence level) smaller in size than those occurring in all other months, with December in general featuring the largest events and June the smallest (Fig. 8a). The mean values of average precipitation, maximum precipitation amount, and duration for nontropical EPEs display relative minima in January, July, and November and relative maxima in spring (April or May) and autumn (September or October; Figs. 8b–d). For both average precipitation and duration, the January and July means are significantly different (above the 95% confidence level) from the means for the two months corresponding to the spring and autumn maxima; for
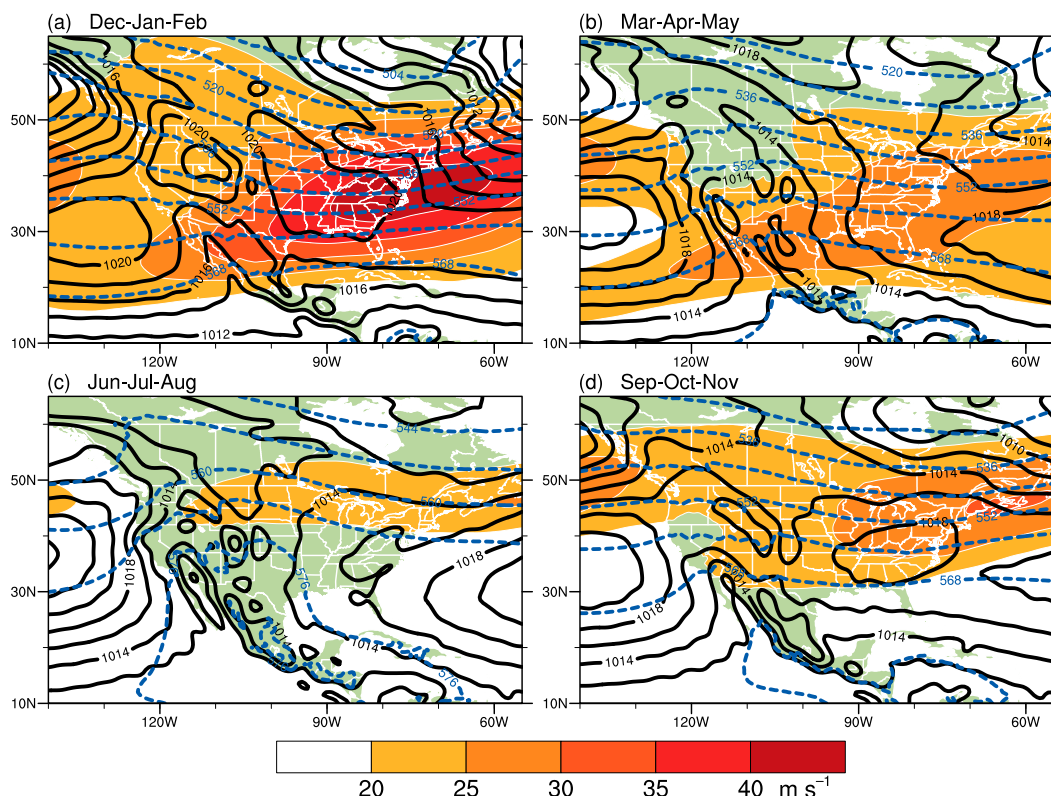
FIG. 6. Long-term (1979–2010) seasonal mean 250-hPa wind speed (shaded in m s^{-1} according to the color bar), 1000–500-hPa thickness (contoured in blue every 8 dam), and sea level pressure (contoured in black every 2 hPa) for (a) DJF, (b) MAM, (c) JJA, and (d) SON computed from the CFSR.

maximum precipitation amount, only the January mean is significantly different.

To establish physical context for the observed attributes of nontropical EPEs, we now examine environmental parameters that are representative of key ingredients for heavy rainfall (Fig. 9). Specifically, we examine IVT, 850-hPa **Q**-vector convergence (used here as a proxy for QG forcing for vertical motion; Hoskins et al. 1978), PW, and surface-based CAPE. The values of these parameters, derived from the CFSR, were first averaged over the 24-h (1200–1200 UTC) period corresponding to the EPE, and for each parameter except CAPE, the 24-h average values were spatially averaged over a 5° latitude × 5° longitude box centered on the CFSR grid point closest to the location of maximum 24-h precipitation associated with the EPE. The maximum value, rather than the spatially averaged value, was used for CAPE as this value tended to better represent the instability in the EPE environment.

The values of the parameters pertaining to dynamical influences, IVT, and **Q**-vector convergence, tended to be lower in JJA than in all other months of the year and on average peaked in December and February, respectively (Figs. 9a,b). Conversely, the thermodynamic

parameters, PW and CAPE, tended to be highest in the summer and lowest in the winter (Figs. 9c,d). The differences between the JJA means and the DJF means for the four parameters in Fig. 9 are all (except January **Q**-vector convergence) statistically significant above the 95% confidence level. These results demonstrate that, consistent with the seasonality of the
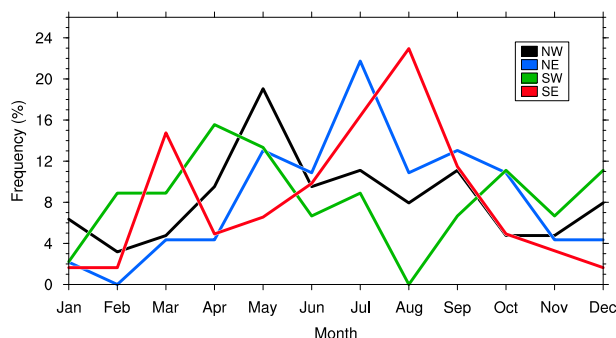

FIG. 7. The monthly distributions of nontropical EPEs separated by region. Frequency values are expressed as a percent of the total number of nontropical EPEs that occurred in the corresponding region. The lines are colored according to the legend.
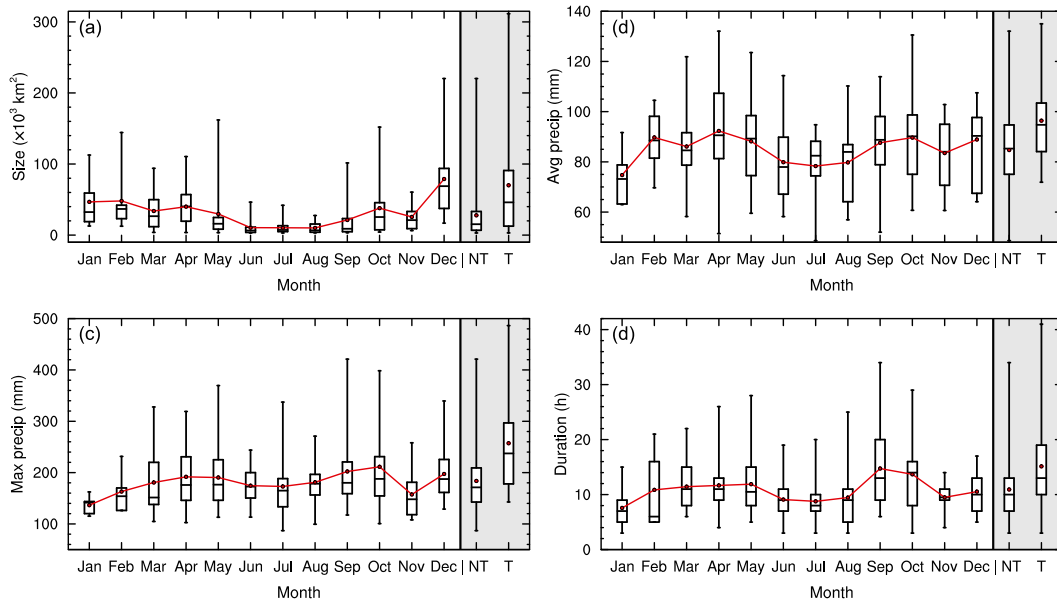
FIG. 8. Box-and-whisker plots of (a) EPE size (10^3 km^2), (b) average precipitation over all grid points associated with the EPE (mm), (c) maximum 24-h precipitation (mm), and (d) duration (h). Plots are shown for nontropical EPEs separated by month as well as for all nontropical and all tropical EPEs (rightmost two in the gray-shaded region; labeled "NT" and "T," respectively). For each box-and-whisker element, the lower and upper bounds of the boxed area are drawn at the 25th and 75th percentiles, respectively, the center line between the lower and upper boxes denotes the median value, the red dots and adjoining red line mark the mean value, and the whiskers indicate the minimum and maximum values.

midlatitude baroclinic zone and the jet stream over the United States (Fig. 6), cool-season EPEs tend to involve stronger dynamical processes, whereas warm-season EPEs tend to involve more abundant water vapor and greater conditional instability in the absence of strong dynamical processes.

4. Synoptic-scale composites of nontropical EPEs

a. Composites for all nontropical EPEs

Although subtle differences were evident, the synoptic-scale configurations displayed in the size-based and IVT-based composites for all nontropical EPEs were found to be markedly similar. Specifically, the "large scale" and "small scale" EPE composites were found to exhibit marked similarities to the "strong IVT" and "weak IVT" EPE composites, respectively. Because of these similarities, the size-based and IVT-based composites are discussed concurrently in this subsection, and only maps for the IVT-based composites are shown (Fig. 10).

The large-scale and strong-IVT composites feature a statistically significant (>95% confidence; Fig. 11a) high-amplitude upper-level trough–ridge pattern, with the EPE positioned on the anticyclonic shear side of a southwesterly 50 m s^{-1} jet streak, in the presence of 20–25 m s^{-1} 1000–500-hPa shear, and in an area of warm

advection within the warm sector of a surface cyclone (Figs. 10a,c,g). The anticyclonic shear side of an upper-level jet is a favored location for weak inertial stability, a condition that can favor upscale growth of MCSs (e.g., Emanuel 1979; Blanchard et al. 1998; Coniglio et al. 2010). It is possible that EPEs can be influenced by areas of weak inertial stability; however, more work is needed to quantify this effect.

Relative to the large-scale and strong-IVT composites, the small-scale and weak-IVT composites feature weaker and lower-amplitude upper-level flow that is generally not statistically different from climatology. The EPE is positioned in a region of $\sim$5 m s^{-1} 1000–500-hPa shear, on the warm side of a baroclinic zone, and on the western flank of a broad subtropical high (Figs. 10b,d,h). The precipitation distribution in the large-scale and strong-IVT composites exhibits an expansive linearly organized structure (Fig. 10a) aligned with the 1000–500-hPa shear (Fig. 10g), whereas that in the small-scale and weak-IVT composites is relatively localized and lacks coherent organization (Fig. 10b), consistent with the weak 1000–500-hPa shear in the vicinity of the EPE (Fig. 10h).

In the large-scale and strong-IVT EPE composite environments, an elongated corridor of strong (15 m s^{-1}) 925-hPa winds (i.e., LLJ), associated with warm
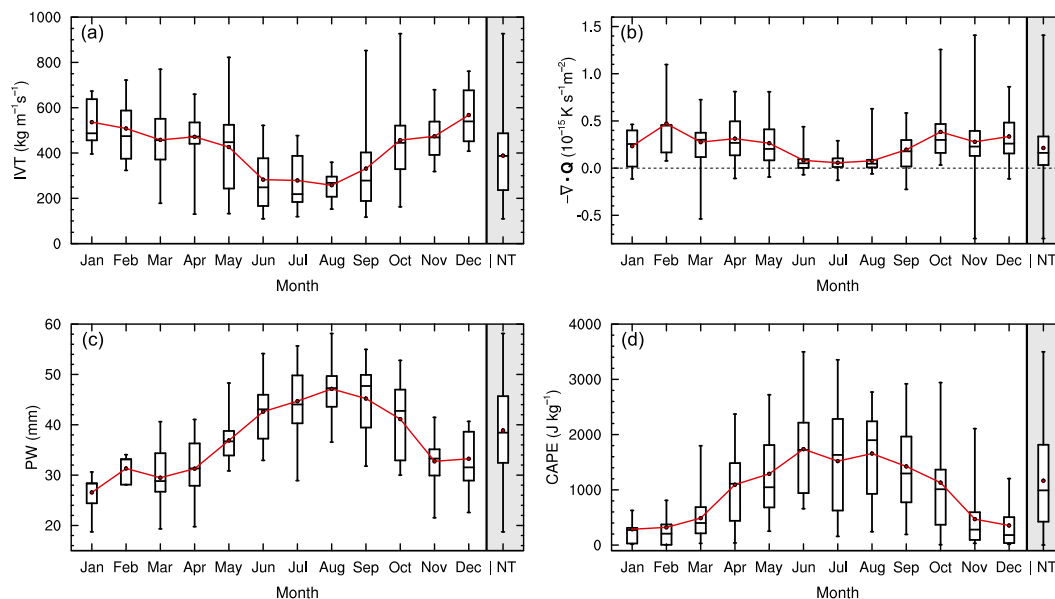
FIG. 9. As in Fig. 8, but showing (a) IVT (kg m^{-1} s^{-1}), (b) 850-hPa **Q**-vector convergence [10^{-15} K s^{-1} m^{-2}; positive (negative) values indicate forcing for ascent (descent)], (c) PW (mm), and (d) CAPE (J kg^{-1}), and not including tropical EPEs.

advection and strong ($>$600 kg m^{-1} s^{-1}) IVT, extends poleward from low latitudes into the EPE region, coincident with a large sea level pressure (SLP) gradient between the surface cyclone and a prominent anticyclone to the east (Figs. 10c,e). Within this corridor, moist, conditionally unstable air, characterized by PW values of 30–40 mm and CAPE values of 250–1000 J kg^{-1}, is transported into the EPE region (Figs. 10e,g). The region of PW extending poleward across the EPE region and the SLP patterns associated with the cyclone and anticyclone are statistically significant above the 95% confidence level (Fig. 11a).

The small-scale and weak-IVT EPE composite environments exhibit higher CAPE values ($>$1000 J kg^{-1}) and higher PW values ($>$40 mm) through a broad region over and equatorward of the EPE location in the presence of weak IVT ($<$100 kg m^{-1} s^{-1}) and southeasterly low-level flow ($\sim$2.5 m s^{-1}) between a surface trough southwest of the EPE and a surface ridge to the northeast on the cool side of the baroclinic zone (Figs. 10d,f,h). These surface features as well as the PW distribution in the vicinity of the EPE are statistically significant above the 95% confidence level (Fig. 11b).

b. Regional composites

The IVT-based composites constructed for the four separate geographical regions (Figs. 12–15) capture the salient signatures discussed in the previous section. Although the regional composites share many similarities, some statistically significant differences exist between them (Fig. 16). An important caveat regarding the regional composites is that some of the characteristics therein may not represent distinctive regional signatures but rather, consistent with the small sample size for each composite, simply reflect the characteristics of the individual events within the composites.

The four regional strong-IVT EPE composites feature a high-amplitude upper-level trough–ridge pattern, with an expansive linearly organized area of precipitation situated on the anticyclonic shear side of an anticyclonically curved southwesterly jet streak (Figs. 12a, 13a, 14a, and 15a). The EPE is positioned near the equatorward entrance region of the jet streak (a favorable region for forcing of ascent) in the NW, NE, and SW composites (Figs. 11a, 13a, and 14a), and near the jet core in the SE composite (Figs. 12a and 15a). The 250-hPa geopotential height patterns in the vicinity of the EPE for the four composites are generally not significantly different from each other (Figs. 16a–f).

The NW and SW strong-IVT composites both feature a surface trough/low positioned along the eastern Mexico coast near the base of the upper-level trough (Figs. 12a,c) and a surface low located farther poleward in the vicinity of the EPE near the upper-level jet axis (Figs. 14a,c). The disturbance along the eastern Mexico coast, associated with statistically significant SLP differences relative to the NE and SE composites (Figs. 16a,c,d), could be a signature of a lee trough developing in connection with strong westerly flow across the
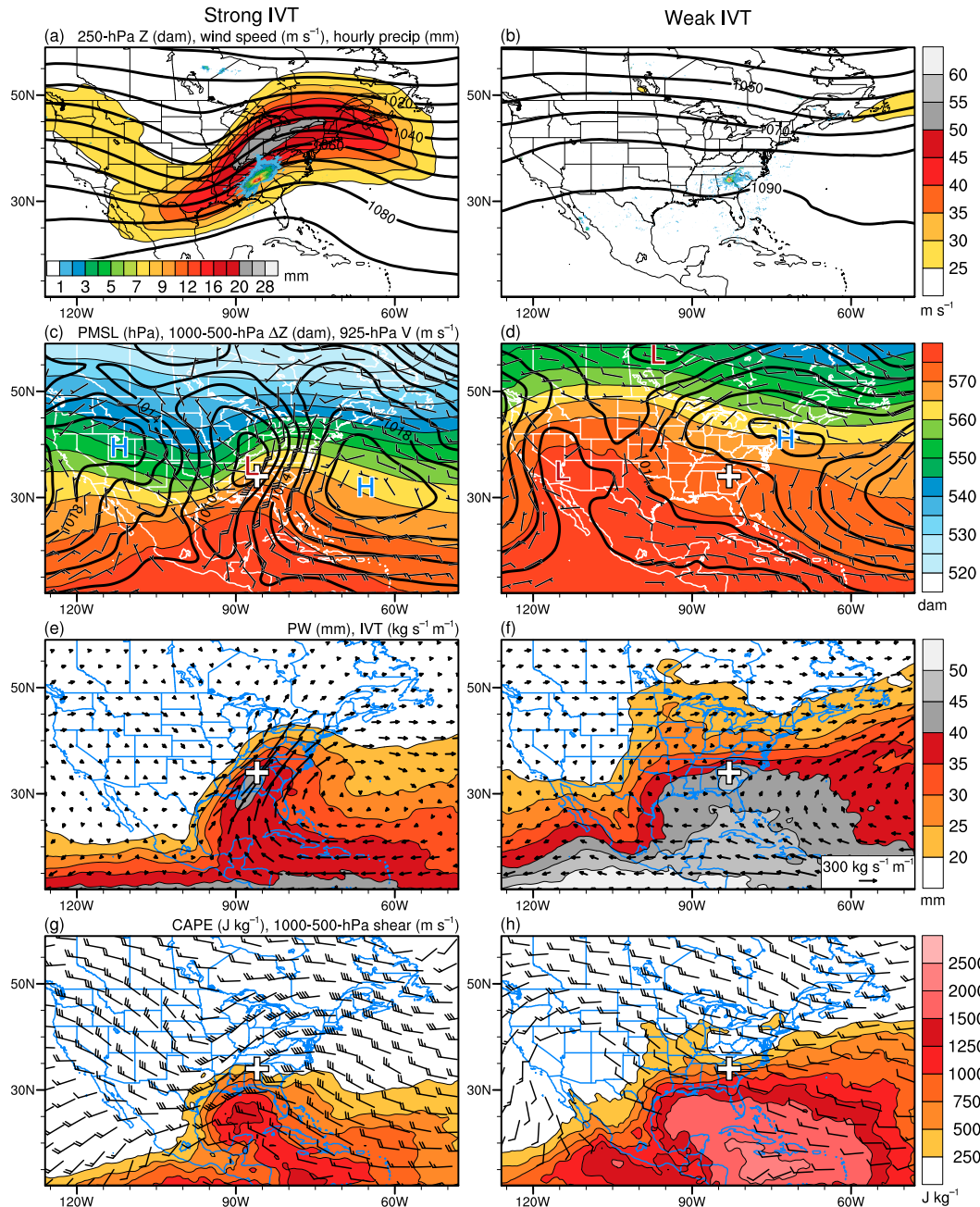
FIG. 10. Composites for the (left) top 50 (strong IVT) and (right) bottom 50 (weak IVT) nontropical EPEs with respect to IVT magnitude showing: (a),(b) 250-hPa geopotential height (contoured in black every 10 dam), wind speed (shaded in m s^{-1} according to the color bar), and stage-IV hourly precipitation [shaded in mm according to the inset color bar in (a)]; (c),(d) SLP (contoured in black every 2 hPa; minima and maxima denoted by the "L" and "H" symbols), 1000–500-hPa thickness (shaded in dam according to the color bar), and 925-hPa wind (plotted for wind speed ≥2.5 m s^{-1}; half barb: 2.5 m s^{-1}; full barb: 5 m s^{-1}; pennant 25 m s^{-1}); (e),(f) PW (shaded in mm according to the color bar) and IVT vectors [kg m^{-1} s^{-1}; reference vector in bottom right of (f)]; and (g),(h) surface-based CAPE (shaded in J kg^{-1} according to the color bar) and 1000–500-hPa wind shear [plotted for shear magnitude ≥5 m s^{-1}; same barb convention as in (c) and (d)]. The plus symbol in (c)–(h) marks the location of the EPE.
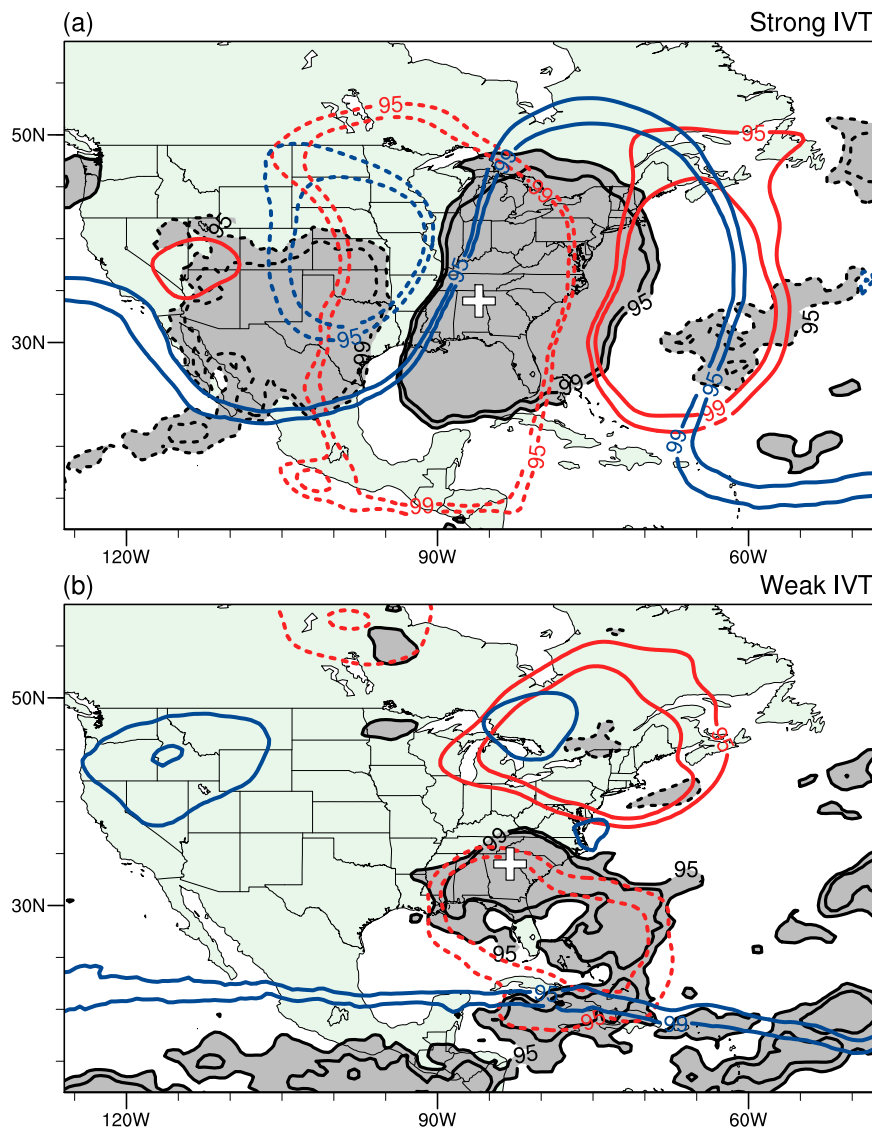
FIG. 11. Statistical significance of 250-hPa geopotential height (contoured in blue), SLP (contoured in red), and PW (shaded in gray and contoured in black) according to a two-sided Student's *t* test for composites of the (a) top 50 and (b) bottom 50 nontropical EPEs with respect to IVT magnitude. The contours indicate areas of >95% and >99% probability that the composite means are statistically different from climatology. Dashed contours denote areas where departures from climatology are negative. The plus symbol marks the location of the EPE.

Mexican Plateau downstream of the upper-level trough as noted by Moore et al. (2012) for the May 2010 Nashville, Tennessee, flood event. For both the NW and SW composites, an elongated corridor of strong confluent poleward low-level flow and IVT extends from low latitudes over the Caribbean Sea and the Gulf of Mexico into the EPE region in association with a strong SLP gradient between the southern surface trough and an anticyclone to the east (Figs. 12c,e and 14c,e). This

corridor is associated with an elongated plume of PW values in excess of 35 mm and an area of CAPE extending into the EPE region (Figs. 12e,g and 14e,g).

The strong-IVT composites for the NE and SE regions exhibit distinct cyclone characteristics. Specifically, in the NE composite, the EPE occurs in connection with a frontal wave along the trailing cold front of a cyclone centered in the northern portion of the composite domain (Fig. 13c). This cyclone is associated with
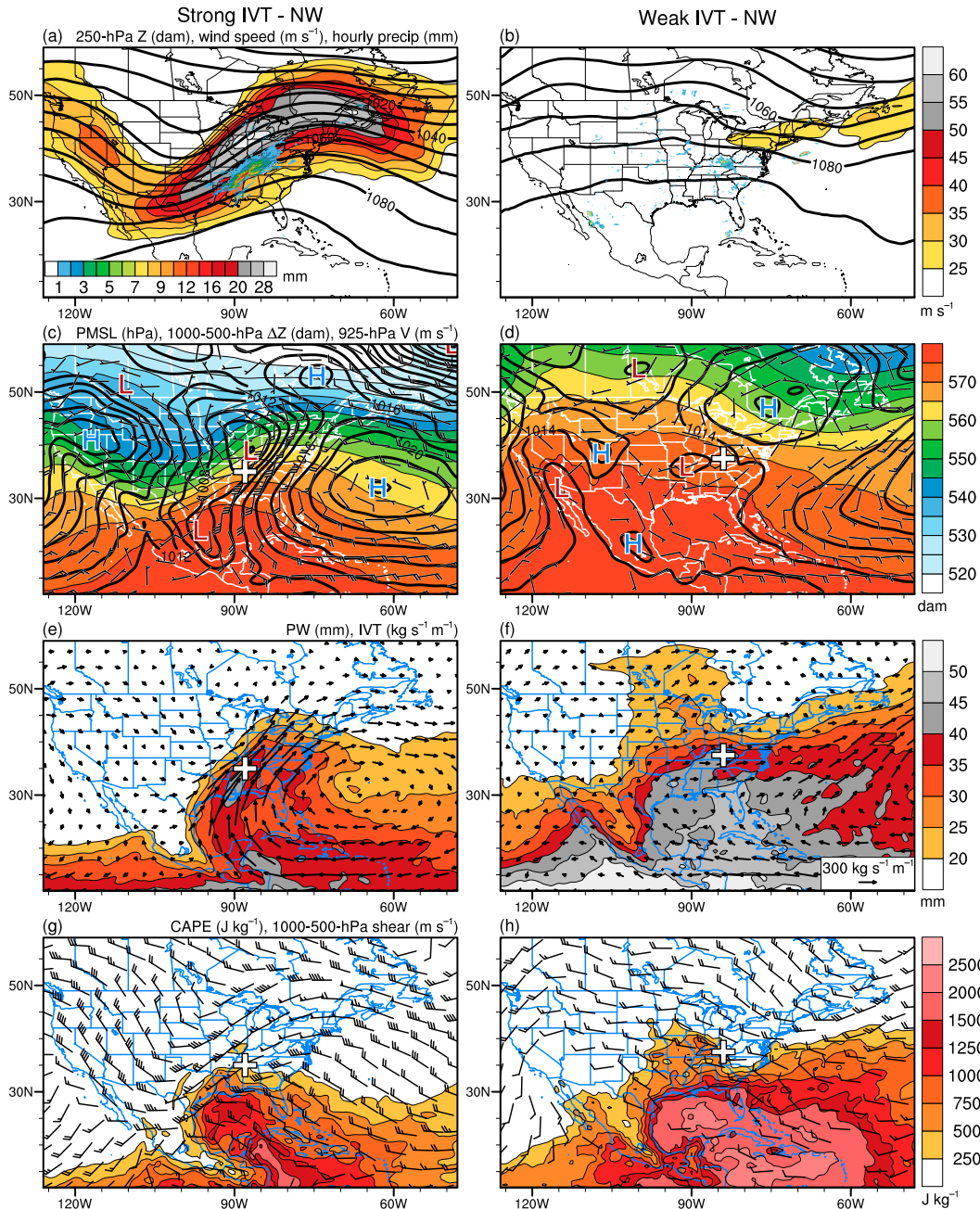
FIG. 12. As in Fig. 11, but for the (left) top quintile and (right) bottom quintile of nontropical EPEs with respect to IVT magnitude occurring within the NW region. Each composite consists of 13 events.

statistically significant SLP differences relative to the NW and SE composites (Figs. 16a,f). In the SE composite, by contrast, the EPE is located near the center of a transient cyclone, with a secondary surface low located to the south (Fig. 15c). Both composites feature a corridor of strong poleward low-level flow and IVT, appearing to draw moist, unstable air from over the Gulf of Mexico and the Atlantic into the EPE region (Figs. 13c,e,g and 15c,e,g). It

is likely that for some EPEs this corridor of low-level flow and IVT is positioned such that it impinges upon the eastern slopes of the Appalachian Mountains, resulting in orographic precipitation enhancement. Time-lagged composites (not shown) indicate that the cyclone in the SE region composite originates in the western Gulf of Mexico and progresses northeastward thereafter, exhibiting a track similar to the cyclone tracks found by
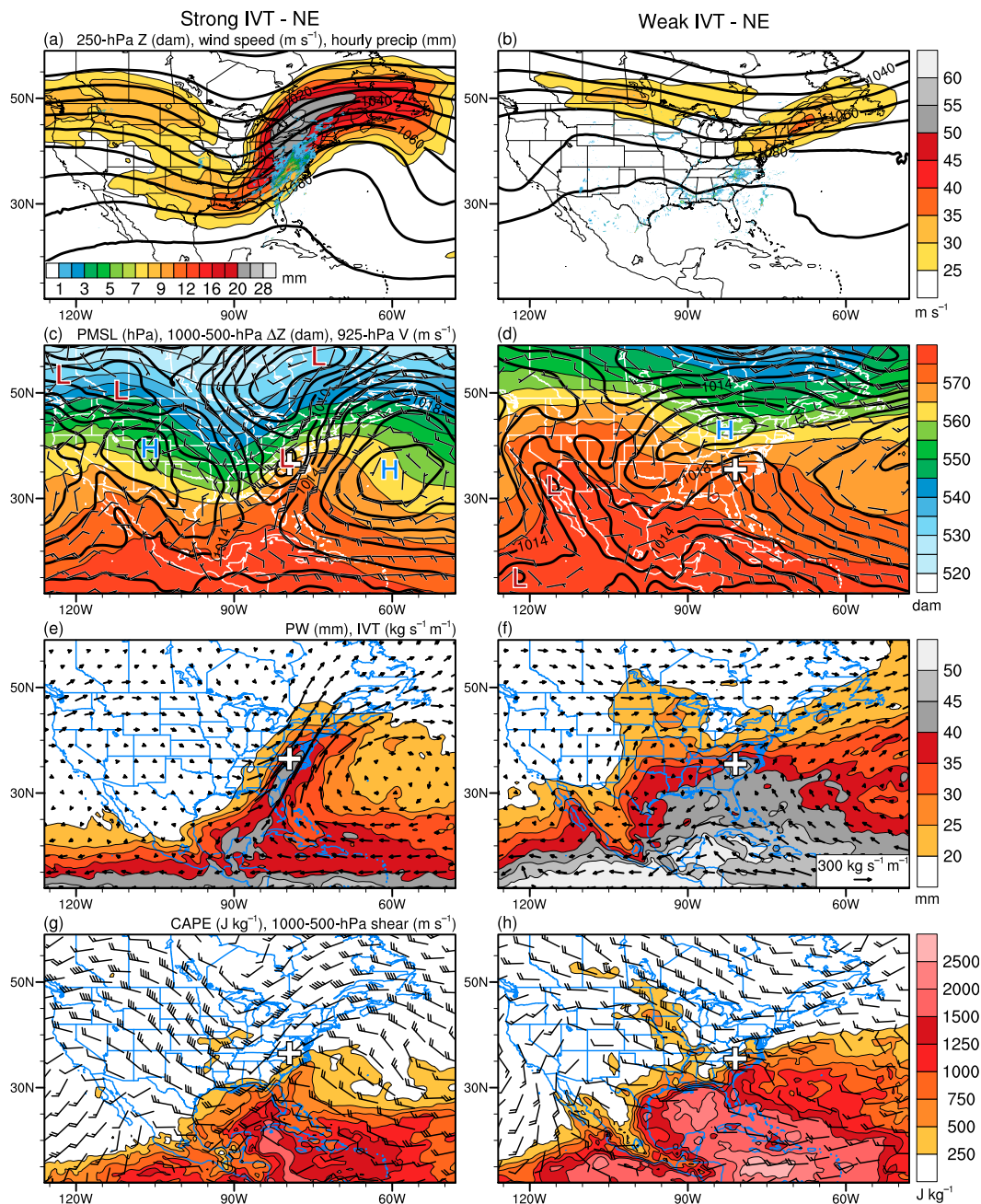
FIG. 13. As in Fig. 12, but for the NE region. Each composite consists of 9 events.

Businger et al. (1990) to be favorable for heavy cool-season precipitation across Georgia and South Carolina.

In the weak-IVT composites for the NW, NE, and SW regions, the EPE, characterized by a relatively disorganized area of precipitation, is positioned downstream of a weak shortwave trough embedded in weak zonal upper-level flow (Figs. 12b, 13b, and 14b). By contrast, the EPE in the SE region composite is located beneath a broad ridge in the presence of weak winds throughout of the

troposphere (Figs. 15b,d,h). The short-wave trough in the SW and NE composites is associated with statistically significant geopotential height differences relative to the NW and SE composites (Figs. 16g,h,k,l). At low levels in the NW, SW, and NE composites, although statistically significant SLP differences are evident (Figs. 16g,h), the EPE is generally positioned within a region of confluent low-level flow near an inverted surface trough on the warm side of a baroclinic zone that is situated
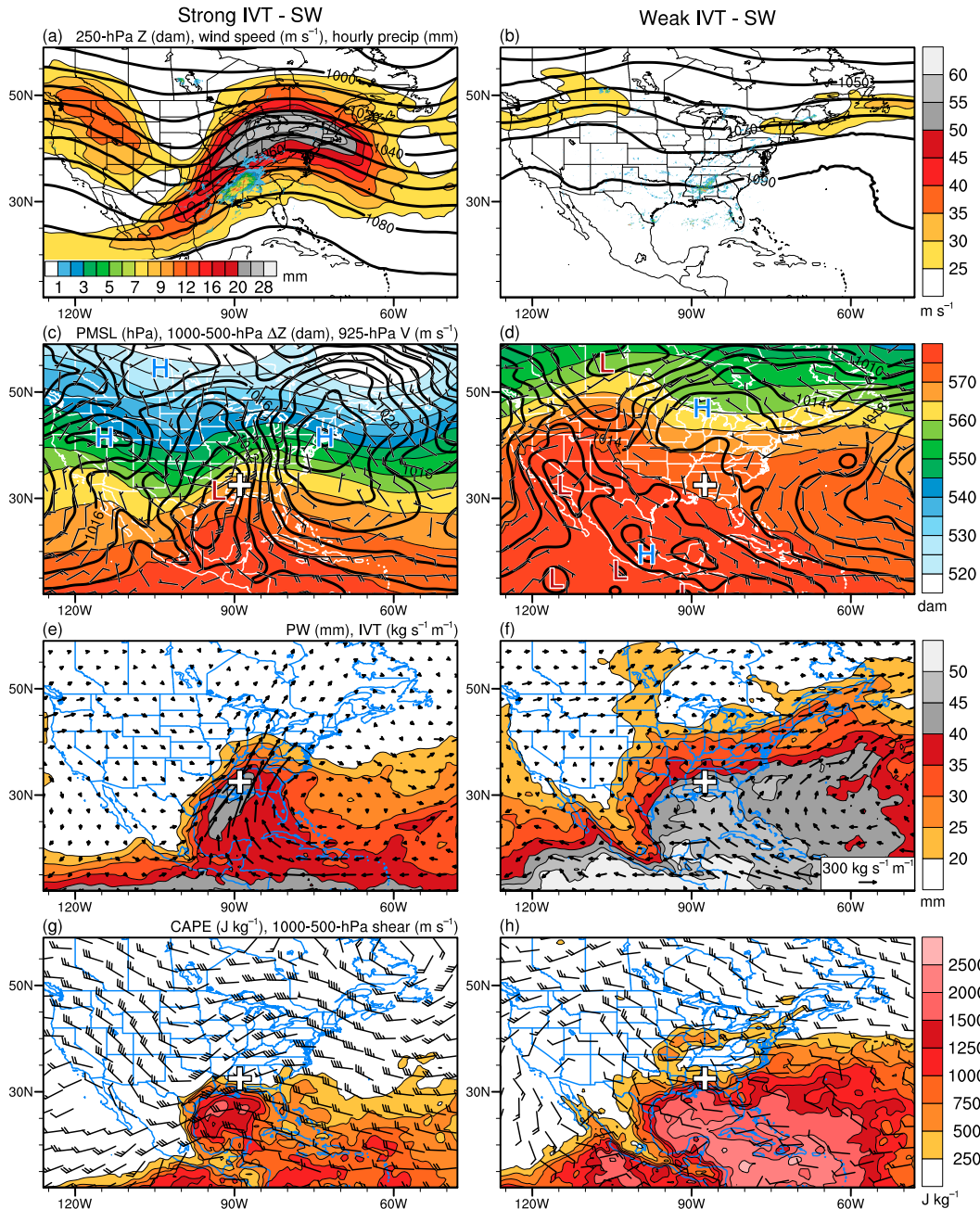
FIG. 14. As in Fig. 12, but for the SW region. Each composite consists of 9 events.

equatorward of a surface ridge/anticyclone (Figs. 12d, 13d, and 14d). Furthermore, weak poleward low-level flow extends into the EPE region between the inverted trough and the subtropical high to the east, contributing to weak transport of moist and conditionally unstable air (Figs. 12f,h, 13f,h, and 14f,h). For the SE composite, the EPE is located well equatorward of a baroclinic zone in the midst of a moist, unstable airmass within a broad area of surface high pressure (Figs. 15d,f,h). Areas of significantly

higher SLP values relative to the NW, SW, and NE composites are found to the south of the EPE (Figs. 16i,k,l).

5. Forecast skill associated with EPEs

Based upon prior research (e.g., Stensrud and Fritsch 1994; Jankov and Gallus 2004; Hohenegger et al. 2006; Keil et al. 2014), we hypothesize that numerical model QPF skill is greater for strong-IVT
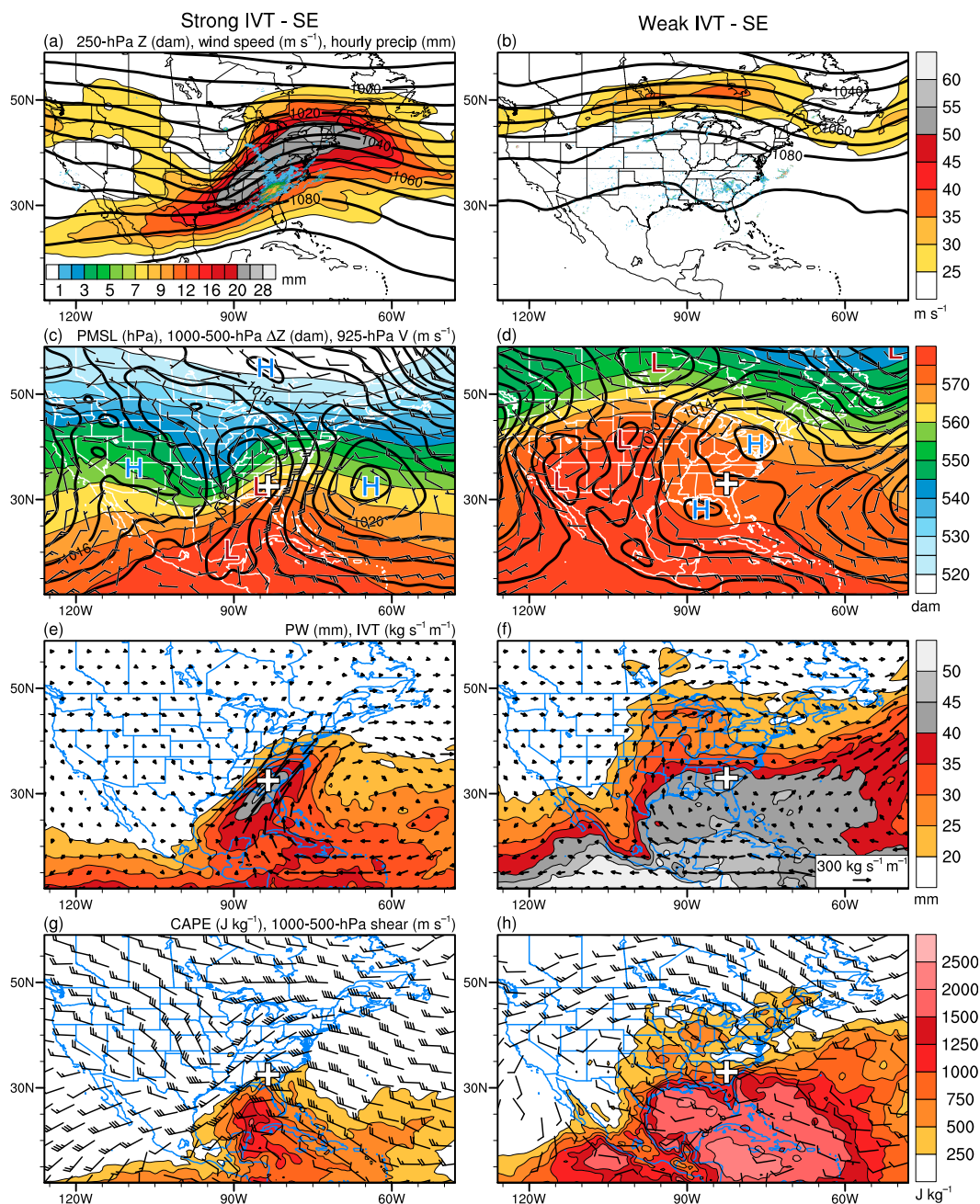
FIG. 15. As in Fig. 12, but for the SE region. Each composite consists of 12 events.

EPEs than for weak-IVT EPEs. To test our hypothesis, deterministic 24-h precipitation accumulation forecasts from the GEFS reforecast control member at 36-, 84-, and 132-h lead times were assessed for the top 50 and bottom 50 nontropical EPEs with respect to IVT magnitude using the equitable threat score (ETS; Figs. 17a–c; Schaefer 1990) and multiplicative bias (BIA; Figs. 17d–f; Wilks 2011). The fraction of CCPA grid points inside the SEUS domain with observed

precipitation in exceedance of a given threshold is also shown for reference (Fig. 17g). The analysis in this section demonstrates the type of EPE-related QPF analysis that could be further undertaken in support of the objectives of HMT-SE.

In agreement with our hypothesis, the ETS plots (Figs. 17a–c) reveal greater skill at all precipitation thresholds and all lead times for the strong-IVT category relative to the weak-IVT category. The difference in
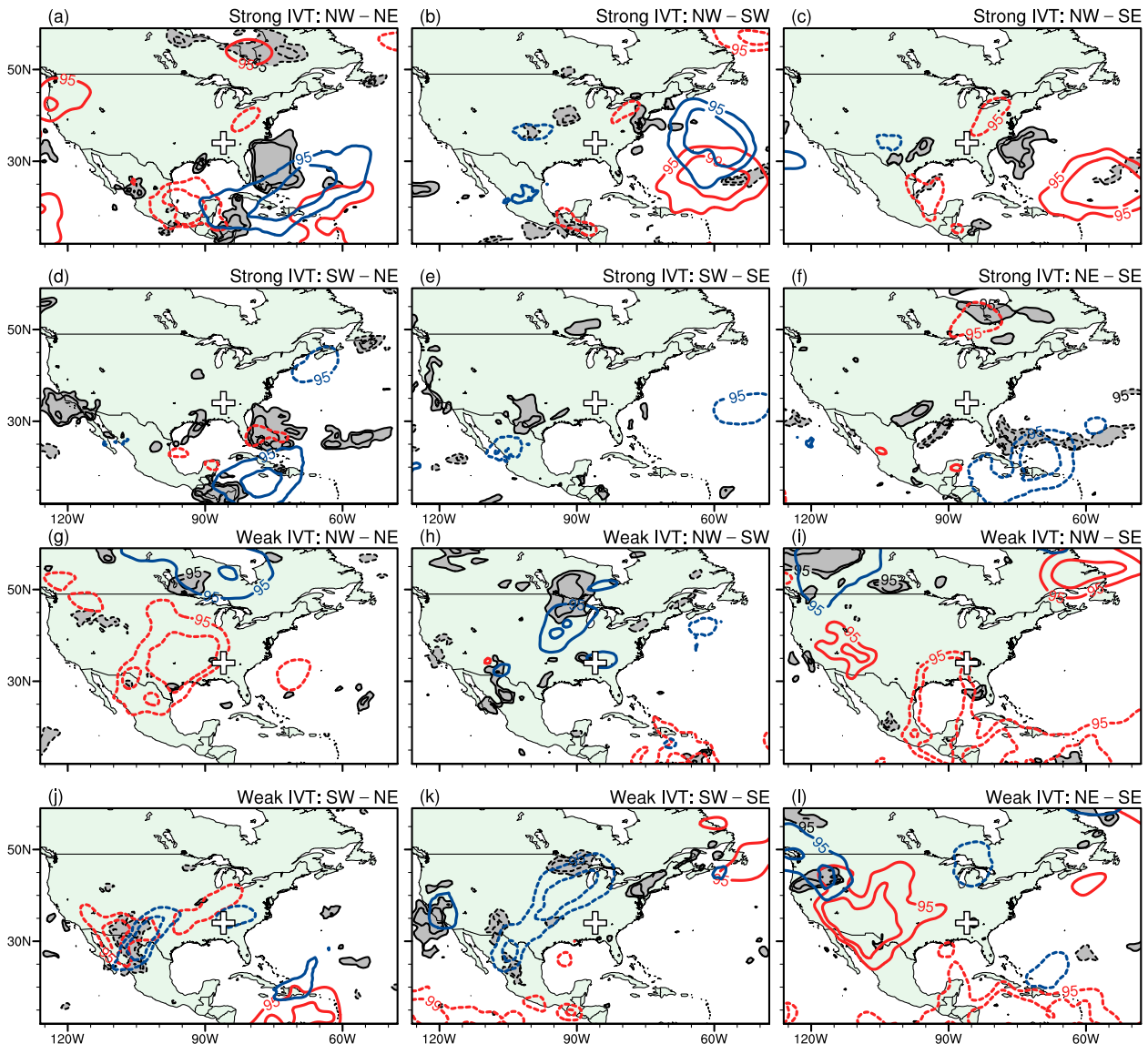
FIG. 16. Statistical significance of 250-hPa geopotential height (contoured in blue), SLP (contoured in red), and PW (shaded in gray and contoured in black) according to a two-sided Student's t test for (a)–(f) each pair of strong-IVT regional composites and (g)–(l) each pair of weak-IVT regional composites. The contours indicate areas of >95% and >99% probability that the differences between the (a),(g) NW and NE; (b),(h) NW and SW; (c),(i) NW and SE; (d),(j) SW and NE; (e),(k) SW and SE; and (f),(l) NE and SE composite means are significant. Dashed contours denote areas where differences between the composites are negative. The plus symbol marks the location of the EPE.

skill between the two categories is most pronounced for earlier forecast lead times, with ETS for both categories approaching zero skill as lead time increases beyond 132 h (not shown). The ETS generally decreases with increasing precipitation threshold but unexpectedly indicates considerably lower forecast skill at the 0.1-mm threshold relative to higher thresholds (1–5 mm) for the strong-IVT category. This unexpected result is possibly due to an overforecast bias at the 0.1-mm threshold (Figs. 17d–f), but could

also relate to deficiencies of the CCPA in capturing very light precipitation amounts.[2]

The strong-IVT and weak-IVT categories are both associated with BIA values below one at precipitation thresholds above 10 mm, indicating an underforecast bias (Figs. 17d–f). Consistent with the differences in the ETS

---

[2] Hamill (1999) found that under some circumstances an overforecast bias can result in inflated ETS values.
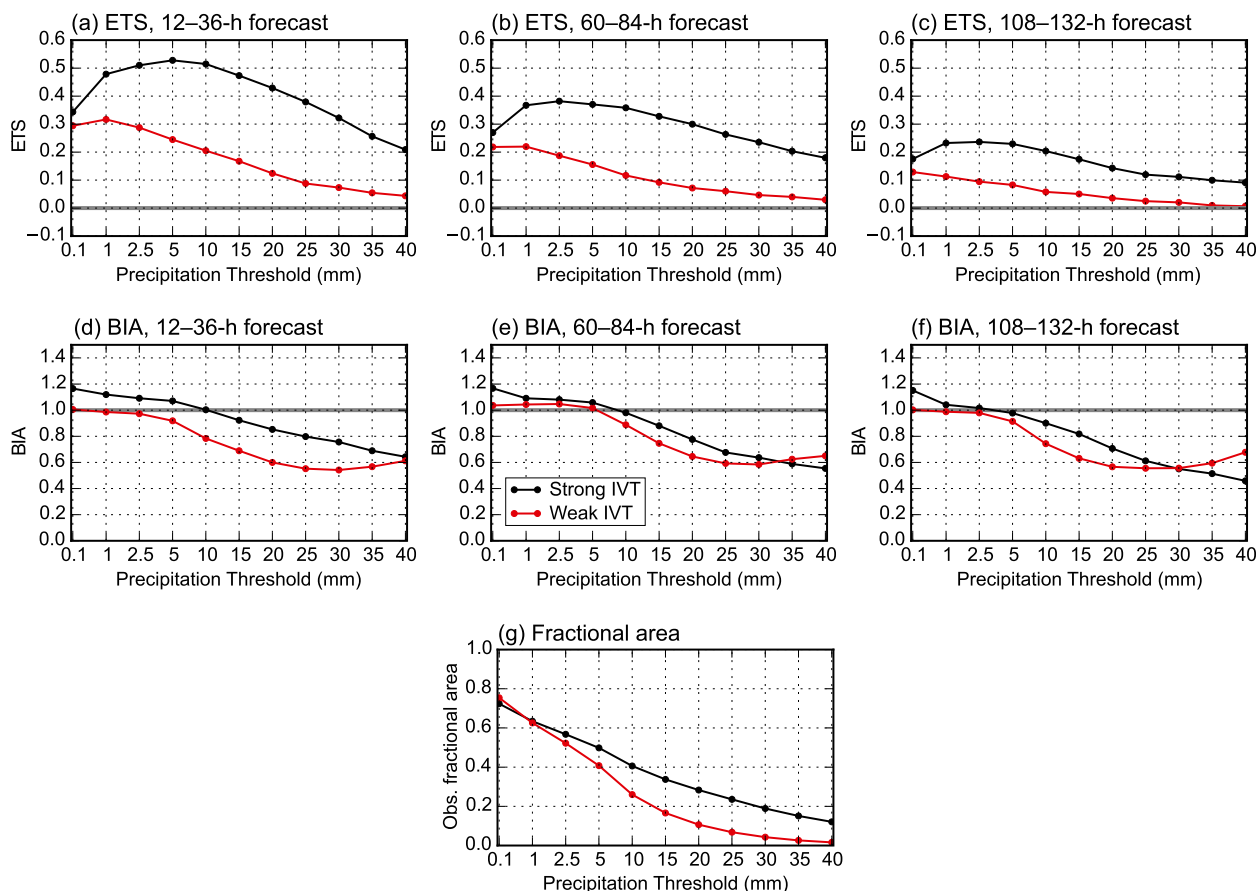
FIG. 17. Plots of (a)–(c) ETS and (d)–(f) BIA for deterministic 24-h accumulated precipitation forecasts at (left) 36-h, (middle) 84-h, and (right) 132-h lead time from the GEFS reforecast control member for the top 50 (black) and bottom 50 (red) nontropical EPEs with respect to IVT magnitude. (g) The fraction of grid points from the CCPA analyses with observed precipitation exceeding a given threshold is shown for both groups of EPEs.

between the two categories, the BIA values for the strong-IVT category are greater (i.e., closer to one) than those for the weak-IVT category at precipitation amounts above 10 mm (except above 30 mm at 84- and 132-h lead time). Weak-IVT EPEs are nearly always associated with smaller areas of precipitation than strong-IVT EPEs (Fig. 17g), suggesting that QPF skill for weak-IVT EPEs is more sensitive to relatively small position errors. Therefore, the differences in areal coverage of precipitation could contribute to the QPF skill disparity between the two categories indicated by the ETS and BIA. Such impacts of areal coverage on QPF skill could be mitigated through the use of object-based forecast verification methods (e.g., Davis et al. 2006).

6. Discussion and conclusions

In this study, a 10-yr (2002–11) climatology of EPEs in the southeastern United States was constructed using

24-h multisensor precipitation analyses from the NCEP stage-IV dataset. An object-based approach was applied to the stage-IV analyses to identify spatially coherent EPEs encompassing a variety of event sizes and types. The approach used in the current study is similar to object-based approaches applied in previous studies (e.g., Davis et al. 2006; Hitchens et al. 2012); however, rather than using a fixed precipitation threshold for identifying precipitation objects, we used geographically varying thresholds based upon the 99th percentile and 99.9th percentile of 24-h precipitation at each grid point.

The characteristics of the EPEs in the climatology were analyzed in detail. Salient results of the analysis are as follows:

- Tropical EPEs, while not as common as nontropical EPEs, tended to be larger, more intense (i.e., larger rainfall amounts), and longer lived than nontropical EPEs, underscoring their potential to cause significant

flooding (e.g., Villarini and Smith 2010; Villarini et al. 2014).

- Consistent with previous studies on the precipitation contributions of TCs in the SEUS (e.g., Knight and Davis 2007, 2009; Shepherd et al. 2007; Prat and Nelson 2013), tropical EPEs occurred exclusively in summer and autumn and most frequently affected the eastern portion of the domain, especially along the eastern slopes of the Appalachian Mountains and along the coast.
- In general agreement with the results of Keim (1996) and Prat and Nelson (2014), nontropical EPEs most frequently affected the western portion of the SEUS domain during the winter and spring and the eastern portion during summer.
- Nontropical EPEs are characterized by considerable variability with regard to precipitation amounts and environmental characteristics. In general, EPE size maximized in the winter and minimized in the summer. Correspondingly, IVT and **Q**-vector convergence (i.e., dynamical influences) associated with EPEs both tended to be highest in winter and lowest in summer, whereas the opposite was evident for CAPE and PW (i.e., thermodynamical influences). Precipitation amounts and duration were generally largest for spring and autumn EPEs, perhaps reflecting the coincidence of relatively strong dynamical and thermodynamical influences during those seasons.

Composites based upon EPE size and IVT magnitude reveal that "large scale" and "strong IVT" EPEs characteristically occur within high-amplitude synoptic-scale flow patterns including 1) an upper-level trough–ridge pattern associated with strong deep-layer shear over the EPE region and a strong southwesterly jet streak immediately poleward of the EPE location; 2) a focused corridor of strong poleward low-level flow, associated with warm-air advection and strong IVT, that extends into the EPE region within the warm sector of a surface cyclone and on the western flank of a prominent anticyclone; and 3) a plume of high PW values and an area of CAPE extending into the EPE region along the corridor of poleward flow. For these types of EPEs, the continuous replenishment of water vapor and conditional instability afforded by the synoptic-scale flow can help sustain widespread heavy precipitation over a given region, resulting in expansive areas extreme precipitation accumulations. Such a scenario is exemplified by the May 2010 Nashville, Tennessee, flood event documented by Moore et al. (2012) and is conceptualized by the classic Maddox et al. (1979) "synoptic" flash-flood pattern. Given the key role of water vapor transport in producing precipitation in the strong-IVT scenario, it is

conceivable that numerical model QPF skill associated with strong-IVT EPEs is sensitive to forecast errors related to the processes linked to water vapor transport (e.g., Mahoney and Lackmann 2007).

As discussed for the May 2010 Nashville flood event by Moore et al. (2012), the strong-IVT composites for the western two regions (NW and SW) feature a conspicuous lee–trough-like feature east of Mexico, which appears to play a key role in transporting water vapor from low latitudes into the EPE region. For the NE region strong-IVT composite, water vapor transport is forced in association with a frontal wave along the trailing cold front of a cyclone positioned to the north, while the SE composite features water vapor transport within the warm sector of a cyclone that develops over the western Gulf of Mexico and traverses eastward into the SEUS. Given the variability of cyclone characteristics indicated in the regional composites, an examination of preferential cyclone tracks and life cycles associated with EPEs would likely be a worthwhile research direction.

The "small scale" and "weak IVT" EPEs typically occur within low-amplitude synoptic-scale flow patterns featuring 1) relatively weak zonal upper-level flow and weak deep-layer shear, 2) weak poleward low-level flow on the western flank of a subtropical high, 3) a broad area of very moist and conditionally unstable air in the vicinity of the EPE, and 4) a baroclinic zone situated poleward of the EPE. In agreement with previous studies (e.g., Henderson and Vega 1996; Li et al. 2011; Li et al. 2013), the subtropical high appears to often play a key role in transporting moist, unstable air into the environments of small-scale and weak-IVT EPEs. The EPE in the NW, NE, and SW region weak-IVT composites occurs in the vicinity of a weak upper-level shortwave trough and in an area of low-level confluence on the warm side of a baroclinic zone. It is plausible that for some EPEs convection is triggered in connection with boundary layer convergence and lifting at the leading edge of this baroclinic zone. In the SE region composite, the EPE is located beneath a broad ridge in the presence of weak winds throughout the troposphere and well equatorward of a baroclinic zone. In the absence of strong dynamical influences, convection in weak-IVT environments may often be focused near mesoscale surface convergence zones or boundaries (e.g., Koch and Ray 1997), possibly associated with topographic processes (e.g., sea-breeze circulations, cold-air damming) or surface cold pools from prior convection.

As evidenced by the composite analysis in this paper, weakly forced EPE environments, in contrast to those that are strongly forced, commonly do not contain prominent synoptic-scale dynamical features (e.g.,

upper-level trough, surface cyclone, corridor of IVT) that dictate where and when heavy convective precipitation is likely to occur. Weakly forced EPE scenarios can, therefore, be associated exceptional QPF challenges. Accordingly, verification of deterministic precipitation forecasts from the GEFS reforecast dataset revealed that weak-IVT EPEs were in aggregate associated with lower QPF skill than strong-IVT EPEs.

We conclude by noting that the methods and results of the current study can serve as a basis for future research related to EPEs in the SEUS and elsewhere. The methods applied to identify and examine EPEs in the SEUS can be adapted for use in other geographical regions and with other gridded precipitation datasets. Moreover, research aimed at applying different approaches for categorizing or stratifying EPEs would likely be helpful for elucidating other aspects of EPEs. Future research endeavors could expand on the brief forecast verification analysis in this study by identifying EPEs and associated phenomena (e.g., MCSs, TCs, baroclinic cyclones) that were forecast particularly well or particularly poorly. For poorly forecast cases, sensitivity experiments could be conducted to determine ways of improving model forecast skill. Such experiments could entail testing the impact of different model resolutions, assimilation procedures, or parameterization schemes on forecast skill.

REFERENCES

Atallah, E. H., and L. F. Bosart, 2003: The extratropical transition and precipitation distribution of Hurricane Floyd (1999). *Mon. Wea. Rev.,* **131,** 1063–1081, doi:10.1175/1520-0493(2003)131<1063:TETAPD>2.0.CO;2.

Bailey, C. M., G. Hartfield, G. M. Lackmann, K. Keeter, and S. Sharp, 2003: An objective climatology, classification scheme, and assessment of sensible weather impacts for Appalachian cold-air damming. *Wea. Forecasting,* **18,** 641–661, doi:10.1175/1520-0434(2003)018<0641:AOCCSA>2.0.CO;2.

Bell, G. D., and L. F. Bosart, 1988: Appalachian cold-air damming. *Mon. Wea. Rev.,* **116,** 137–161, doi:10.1175/1520-0493(1988)116<0137:ACAD>2.0.CO;2.

Beven, J. L., and Coauthors, 2008: Atlantic hurricane season of 2005. *Mon. Wea. Rev.,* **136,** 1109–1173, doi:10.1175/2007MWR2074.1.

Blanchard, D. O., W. R. Cotton, and J. M. Brown, 1998: Mesoscale circulation growth under conditions of weak inertial instability. *Mon. Wea. Rev.,* **126,** 118–140, doi:10.1175/1520-0493(1998)126<0118:MCGUCO>2.0.CO;2.

Brooks, H. E., and D. J. Stensrud, 2000: Climatology of heavy rain events in the United States from hourly precipitation observations. *Mon. Wea. Rev.,* **128,** 1194–1201, doi:10.1175/1520-0493(2000)128<1194:COHREI>2.0.CO;2.

Browning, K. A., 1990: Organization of clouds and precipitation in extratropical cyclones. *Extratropical Cyclones: The Erik Palmen Memorial Volume,* C. W. Newton and E. O. Holopainen, Eds., Amer. Meteor. Soc., 129–154.

Businger, S., D. I. Knapp, and G. F. Watson, 1990: Storm following climatology of precipitation associated with winter cyclones originating over the Gulf of Mexico. *Wea. Forecasting,* **5,** 378–403, doi:10.1175/1520-0434(1990)005<0378:SFCOPA>2.0.CO;2.

Carbone, R. E., and J. D. Tuttle, 2008: Rainfall occurrence in the U.S. warm season: The diurnal cycle. *J. Climate,* **21,** 4132–4146, doi:10.1175/2008JCLI2275.1.

——, ——, D. Ahijevych, and S. B. Trier, 2002: Inferences of predictability associated with warm season precipitation episodes. *J. Atmos. Sci.,* **59,** 2033–2056, doi:10.1175/1520-0469(2002)059<2033:IOPAWW>2.0.CO;2.

Coniglio, M. C., J. Y. Hwang, and D. J. Stensrud, 2010: Environmental factors in the upscale growth and longevity of MCSs derived from rapid update cycle analyses. *Mon. Wea. Rev.,* **138,** 3514–3539, doi:10.1175/2010MWR3233.1.

Davis, C., B. Brown, and R. Bullock, 2006: Object-based verification of precipitation forecasts. Part I: Methodology and application to mesoscale rain areas. *Mon. Wea. Rev.,* **134,** 1772–1784, doi:10.1175/MWR3145.1.

Emanuel, K. A., 1979: Inertial instability and mesoscale convective systems. Part I: Linear theory of inertial instability in rotating viscous fluids. *J. Atmos. Sci.,* **36,** 2425–2449, doi:10.1175/1520-0469(1979)036<2425:IIAMCS>2.0.CO;2.

Evans, J. S., and C. A. Doswell III, 2001: Examination of derecho environments using proximity soundings. *Wea. Forecasting,* **16,** 329–342, doi:10.1175/1520-0434(2001)016<0329:EODEUP>2.0.CO;2.

Franklin, J. L., R. J. Pasch, L. A. Avila, J. L. Beven II, M. B. Lawrence, S. R. Stewart, and E. S. Blake, 2006: Atlantic hurricane season of 2004. *Mon. Wea. Rev.,* **134,** 981–1025, doi:10.1175/MWR3096.1.

Fritsch, J. M., and R. E. Carbone, 2004: Improving quantitative precipitation forecasts in the warm season. *Bull. Amer. Meteor. Soc.,* **85,** 955–965, doi:10.1175/BAMS-85-7-955.

Galarneau, T. J., Jr., L. F. Bosart, and R. S. Schumacher, 2010: Predecessor rain events ahead of tropical cyclones. *Mon. Wea. Rev.,* **138,** 3272–3297, doi:10.1175/2010MWR3243.1.

Hamill, T. M., 1999: Hypothesis tests for evaluating numerical precipitation forecasts. *Wea. Forecasting,* **14,** 155–167, doi:10.1175/1520-0434(1999)014<0155:HTFENP>2.0.CO;2.

——, 2012: Verification of TIGGE multimodel and ECMWF reforecast-calibrated probabilistic precipitation forecasts over the contiguous United States. *Mon. Wea. Rev.,* **140,** 2232–2252, doi:10.1175/MWR-D-11-00220.1.

——, G. T. Bates, J. S. Whitaker, D. R. Murray, M. Fiorino, T. J. Galarneau Jr., Y. Zhu, and W. Lapenta, 2013: NOAA's second-generation global medium-range ensemble reforecast dataset. *Bull. Amer. Meteor. Soc.,* **94,** 1553–1565, doi:10.1175/BAMS-D-12-00014.1.

Henderson, K. G., and A. J. Vega, 1996: Regional precipitation variability in the southern United States. *Phys. Geogr.,* **17,** 93–112, doi:10.1080/02723646.1996.10642576.

Hershfield, D. M., 1961: Rainfall frequency atlas of the United States. U.S. Department of Commerce, Weather Bureau Tech. Paper 40, 115 pp.

Higgins, R. W., J. E. Janowiak, and Y.-P. Yao, 1996: A gridded hourly precipitation data base for the United States (1963–1993). *NCEP/Climate Prediction Center Atlas 1,* U.S. Department of Commerce, NOAA/NSW, 47 pp.

Hitchens, N. M., M. E. Baldwin, and R. J. Trapp, 2012: An object-oriented characterization of extreme precipitation-producing convective systems in the midwestern United States. *Mon. Wea. Rev.,* **140,** 1356–1366, doi:10.1175/MWR-D-11-00153.1.

——, H. E. Brooks, and R. S. Schumacher, 2013: Spatial and temporal characteristics of heavy hourly rainfall in the United States. *Mon. Wea. Rev.,* **141,** 4564–4575, doi:10.1175/MWR-D-12-00297.1.

Hohenegger, C., D. Lüthi, and C. Schär, 2006: Predictability mysteries in cloud-resolving models. *Mon. Wea. Rev.,* **134,** 2095–2107, doi:10.1175/MWR3176.1.

Hoskins, B. J., I. Draghici, and H. C. Davies, 1978: A new look at the ω-equation. *Quart. J. Roy. Meteor. Soc.,* **104,** 31–38, doi:10.1002/qj.49710443903.

Hou, D., and Coauthors, 2014: Climatology-calibrated precipitation analysis at fine scales: Statistical adjustment of stage IV toward CPC gauge-based analysis. *J. Hydrometeor.,* **15,** 2542–2557, doi:10.1175/JHM-D-11-0140.1.

Jankov, I., and W. A. Gallus Jr., 2004: MCS rainfall forecast accuracy as a function of large-scale forcing. *Wea. Forecasting,* **19,** 428–439, doi:10.1175/1520-0434(2004)019<0428:MRFAAA>2.0.CO;2.

Jiang, H., and E. J. Zipser, 2010: Contribution of tropical cyclones to the global precipitation from eight seasons of TRMM data: Regional, seasonal, and interannual variations. *J. Climate,* **23,** 1526–1543, doi:10.1175/2009JCLI3303.1.

Keil, C., F. Heinlein, and G. C. Craig, 2014: The convective adjustment time-scale as indicator of predictability of convective precipitation. *Quart. J. Roy. Meteor. Soc.,* **140,** 480–490, doi:10.1002/qj.2143.

Keim, B. D., 1996: Spatial, synoptic, and seasonal patterns of heavy rainfall in the southeastern United States. *Phys. Geogr.,* **17,** 313–328, doi:10.1080/02723646.1996.10642588.

Knight, D. B., and R. E. Davis, 2007: Climatology of tropical cyclone rainfall in the southeastern United States. *Phys. Geogr.,* **28,** 126–147, doi:10.2747/0272-3646.28.2.126.

——, and ——, 2009: Contribution of tropical cyclones to extreme rainfall events in the southeastern United States. *J. Geophys. Res.,* **114,** D23102, doi:10.1029/2009JD012511.

Knippertz, P., and H. Wernli, 2010: A Lagrangian climatology of tropical moisture exports to the Northern Hemispheric extratropics. *J. Climate,* **23,** 987–1003, doi:10.1175/2009JCLI3333.1.

Koch, S. E., and C. A. Ray, 1997: Mesoanalysis of summertime convergence zones in central and eastern North Carolina. *Wea. Forecasting,* **12,** 56–77, doi:10.1175/1520-0434(1997)012<0056:MOSCZI>2.0.CO;2.

Konrad, C. E., II, 1997: Synoptic-scale features associated with warm season heavy rainfall over the interior southeastern United States. *Wea. Forecasting,* **12,** 557–571, doi:10.1175/1520-0434(1997)012<0557:SSFAWW>2.0.CO;2.

——, 2001: The most extreme precipitation events over the eastern United States from 1950 to 1996: Considerations of scale. *J. Hydrometeor.,* **2,** 309–325, doi:10.1175/1525-7541(2001)002<0309:TMEPEO>2.0.CO;2.

——, and L. B. Perry, 2010: Relationships between tropical cyclones and heavy rainfall in the Carolina region of the USA. *Int. J. Climatol.,* **30,** 522–534, doi:10.1002/joc.1894.

Kunkel, K. E., D. R. Easterling, D. A. R. Kristovich, B. Gleason, L. Stoecker, and R. Smith, 2012: Meteorological causes of the secular variations in observed extreme precipitation events for the conterminous United States. *J. Hydrometeor.,* **13,** 1131–1141, doi:10.1175/JHM-D-11-0108.1.

Lackmann, G. M., 2002: Cold-frontal potential vorticity maxima, the low-level jet, and moisture transport in extratropical cyclones. *Mon. Wea. Rev.,* **130,** 59–74, doi:10.1175/1520-0493(2002)130<0059:CFPVMT>2.0.CO;2.

Lavers, D. A., and G. Villarini, 2013: Atmospheric rivers and flooding over the central United States. *J. Climate,* **26,** 7829–7836, doi:10.1175/JCLI-D-13-00212.1.

Li, L., W. Li, and A. P. Barros, 2013: Atmospheric moisture budget and its regulation of the summer precipitation variability over the Southeastern United States. *Climate Dyn.,* **41,** 613–631, doi:10.1007/s00382-013-1697-9.

Li, W., L. Li, R. Fu, Y. Deng, and H. Wang, 2011: Changes to the North Atlantic subtropical high and its role in the intensification of summer rainfall variability in the southeastern United States. *J. Climate,* **24,** 1499–1506, doi:10.1175/2010JCLI3829.1.

Lin, Y., and K. E. Mitchell, 2005: The NCEP stage II/IV hourly precipitation analyses: Development and applications. *19th Conf. on Hydrology,* San Diego, CA, Amer. Meteor. Soc., 1.2. [Available online at https://ams.confex.com/ams/Annual2005/techprogram/paper_83847.htm.]

Maddox, R. A., C. F. Chappell, and L. R. Hoxit, 1979: Synoptic and meso-scale aspects of flash flood events. *Bull. Amer. Meteor. Soc.,* **60,** 115–123, doi:10.1175/1520-0477-60.2.115.

Mahoney, K. M., and G. M. Lackmann, 2007: The effects of upstream convection on downstream precipitation. *Wea. Forecasting,* **22,** 255–277, doi:10.1175/WAF986.1.

Moore, B. J., P. J. Neiman, F. M. Ralph, and F. E. Barthold, 2012: Physical processes associated with heavy flooding rainfall in Nashville, Tennessee, and vicinity during 1–2 May 2010: The role of an atmospheric river and mesoscale convective systems. *Mon. Wea. Rev.,* **140,** 358–378, doi:10.1175/MWR-D-11-00126.1.

——, L. F. Bosart, D. Keyser, and M. L. Jurewicz, 2013: Synoptic-scale environments of predecessor rain events occurring east of the Rocky Mountains in association with Atlantic basin tropical cyclones. *Mon. Wea. Rev.,* **141,** 1022–1047, doi:10.1175/MWR-D-12-00178.1.

Mullen, S. L., and R. Buizza, 2001: Quantitative precipitation forecasts over the United States by the ECMWF ensemble prediction system. *Mon. Wea. Rev.,* **129,** 638–663, doi:10.1175/1520-0493(2001)129<0638:QPFOTU>2.0.CO;2.

Narapusetty, B., T. DelSole, and M. K. Tippett, 2009: Optimal estimation of the climatological mean. *J. Climate,* **22,** 4845–4859, doi:10.1175/2009JCLI2944.1.

Neiman, P. J., F. M. Ralph, G. A. Wick, Y.-H. Kuo, T.-K. Wee, Z. Ma, G. H. Taylor, and M. D. Dettinger, 2008: Diagnosis of an intense atmospheric river impacting the Pacific Northwest: Storm summary and offshore vertical structure observed with COSMIC satellite retrievals. *Mon. Wea. Rev.,* **136,** 4398–4420, doi:10.1175/2008MWR2550.1.

Newell, R. E., N. E. Newell, Y. Zhu, and C. Scott, 1992: Tropospheric rivers?—A pilot study. *Geophys. Res. Lett.,* **19,** 2401–2404, doi:10.1029/92GL02916.

Parker, M. D., and D. A. Ahijevych, 2007: Convective episodes in the east-central United States. *Mon. Wea. Rev.,* **135,** 3707–3727, doi:10.1175/2007MWR2098.1.

Pfahl, S., and H. Wernli, 2012: Quantifying the relevance of cyclones for precipitation extremes. *J. Climate,* **25,** 6770–6780, doi:10.1175/JCLI-D-11-00705.1.

——, E. Madonna, M. Boettcher, H. Joos, and H. Wernli, 2014: Warm conveyor belts in the ERA-Interim dataset (1979–2010). Part II: Moisture origin and relevance for precipitation. *J. Climate,* **27,** 27–40, doi:10.1175/JCLI-D-13-00223.1.

Pontrelli, M. D., G. Bryan, and J. M. Fritsch, 1999: The Madison County, Virginia, flash flood of 27 June 1995. *Wea. Forecasting,* **14,** 384–404, doi:10.1175/1520-0434(1999)014<0384:TMCVFF>2.0.CO;2.

Prat, O. P., and B. R. Nelson, 2013: Precipitation contribution of tropical cyclones in the southeastern United States from 1998 to 2009 using TRMM satellite data. *J. Climate,* **26,** 1047–1062, doi:10.1175/JCLI-D-11-00736.1.

——, and ——, 2014: Characteristics of annual, seasonal, and diurnal precipitation in the southeastern United States derived from long-term remotely sensed data. *Atmos. Res.,* **144,** 4–20, doi:10.1016/j.atmosres.2013.07.022.

Ralph, F. M., and M. D. Dettinger, 2012: Historical and national perspectives on extreme West Coast precipitation associated with atmospheric rivers during December 2010. *Bull. Amer. Meteor. Soc.,* **93,** 783–790, doi:10.1175/BAMS-D-11-00188.1.

——, P. J. Neiman, and G. A. Wick, 2004: Satellite and CALJET aircraft observations of atmospheric rivers over the eastern North Pacific Ocean during the winter of 1997/98. *Mon. Wea. Rev.,* **132,** 1721–1745, doi:10.1175/1520-0493(2004)132<1721:SACAOO>2.0.CO;2.

——, E. Sukovich, D. Reynolds, M. Dettinger, S. Weagle, W. Clark, and P. J. Neiman, 2010: Assessment of extreme quantitative precipitation forecasts and development of regional extreme event thresholds using data from HMT-2006 and COOP observers. *J. Hydrometeor.,* **11,** 1286–1304, doi:10.1175/2010JHM1232.1.

Saha, S., and Coauthors, 2010: The NCEP Climate Forecast System Reanalysis. *Bull. Amer. Meteor. Soc.,* **91,** 1015–1057, doi:10.1175/2010BAMS3001.1.

Schaefer, J. T., 1990: The critical success index as an indicator of warning skill. *Wea. Forecasting,* **5,** 570–575, doi:10.1175/1520-0434(1990)005<0570:TCSIAA>2.0.CO;2.

Schumacher, R. S., and R. H. Johnson, 2005: Organization and environmental properties of extreme-rain-producing mesoscale convective systems. *Mon. Wea. Rev.,* **133,** 961–976, doi:10.1175/MWR2899.1.

——, and ——, 2006: Characteristics of U.S. extreme rain events during 1999–2003. *Wea. Forecasting,* **21,** 69–85, doi:10.1175/WAF900.1.

——, and C. A. Davis, 2010: Ensemble-based forecast uncertainty analysis of diverse heavy rainfall events. *Wea. Forecasting,* **25,** 1103–1122, doi:10.1175/2010WAF2222378.1.

Shepherd, J. M., A. Grundstein, and T. L. Mote, 2007: Quantifying the contribution of tropical cyclones to extreme rainfall along the coastal southeastern United States. *Geophys. Res. Lett.,* **34,** L23810, doi:10.1029/2007GL031694.

Srock, A. F., and L. F. Bosart, 2009: Heavy precipitation associated with southern Appalachian cold-air damming and Carolina coastal frontogenesis in advance of weak landfalling Tropical Storm Marco (1990). *Mon. Wea. Rev.,* **137,** 2448–2470, doi:10.1175/2009MWR2819.1.

Stensrud, D. J., and J. M. Fritsch, 1994: Mesoscale convective systems in weakly forced large-scale environments. Part III: Numerical simulations and implications for operational forecasting. *Mon. Wea. Rev.,* **122,** 2084–2104, doi:10.1175/1520-0493(1994)122<2084:MCSIWF>2.0.CO;2.

Sukovich, E. M., F. M. Ralph, F. E. Barthold, D. W. Reynolds, and D. R. Novak, 2014: Extreme quantitative precipitation forecast performance at the Weather Prediction Center from 2001 to 2011. *Wea. Forecasting,* **29,** 894–911, doi:10.1175/WAF-D-13-00061.1.

Villarini, G., and J. A. Smith, 2010: Flood peak distributions for the eastern United States. *Water Resour. Res.,* **46,** W06504, doi:10.1029/2009WR008395.

——, R. Goska, J. A. Smith, and G. A. Vecchi, 2014: North Atlantic tropical cyclones and U.S. flooding. *Bull. Amer. Meteor. Soc.,* **95,** 1381–1388, doi:10.1175/BAMS-D-13-00060.1.

Wallace, J. M., 1975: Diurnal variations in precipitation and thunderstorm frequency over the conterminous United States. *Mon. Wea. Rev.,* **103,** 406–419, doi:10.1175/1520-0493(1975)103<0406:DVIPAT>2.0.CO;2.

Wernli, H., and H. C. Davies, 1997: A Lagrangian-based analysis of extratropical cyclones. I: The method and some applications. *Quart. J. Roy. Meteor. Soc.,* **123,** 467–489, doi:10.1002/qj.49712353811.

Wilks, D. S., 2011: *Statistical Methods in the Atmospheric Sciences.* 3rd ed. Academic Press, 676 pp.

Winkler, J. A., B. R. Skeeter, and P. D. Yamamoto, 1988: Seasonal variations in the diurnal characteristics of heavy hourly precipitation across the United States. *Mon. Wea. Rev.,* **116,** 1641–1657, doi:10.1175/1520-0493(1988)116<1641:SVITDC>2.0.CO;2.

Zhang, F., A. M. Odins, and J. W. Nielsen-Gammon, 2006: Mesoscale predictability of an extreme warm-season precipitation event. *Wea. Forecasting,* **21,** 149–166, doi:10.1175/WAF909.1.

Zhu, Y., and R. E. Newell, 1998: A proposed algorithm for moisture fluxes from atmospheric rivers. *Mon. Wea. Rev.,* **126,** 725–735, doi:10.1175/1520-0493(1998)126<0725:APAFMF>2.0.CO;2.